

Original Paper

Cathepsins Drive Anti-Inflammatory Activity by Regulating Autophagy and Mitochondrial Dynamics in Macrophage Foam Cells

Tommy Weiss-Sadan^a David Maimoun^b Diana Oelschlagel^c Farnusch Kaschani^d
Danny Misiak^e Hanmant Gaikwad^a Yael Ben-Nun^a Emmanuelle Merquiol^a
Adi Anaki^a Darya Tsvirkun^a Markus Kaiser^d Patrick Michl^c Israel Gotsman^b
Galia Blum^a

^aInstitute for Drug Research, School of Pharmacy, Faculty of Medicine, The Hebrew University, Jerusalem, Israel, ^bHeart Institute, Hadassah, University Hospital, Jerusalem, Israel, ^cDepartment of Internal Medicine, Martin Luther University, Halle, Germany, ^dDepartment of Chemical Biology, University of Duisburg-Essen, Center for Medical Biotechnology, Faculty of Biology, Essen, Germany, ^eInstitute of Molecular Medicine, Martin Luther University, Halle, Germany

Key Words

Cathepsins • Vascular inflammation • Mitochondrial dynamics • Macrophages • Autophagy

Abstract

Background/Aims: Atherosclerosis underlies the majority of cardiovascular events, consequent to non-resolving inflammation. Considerable evidence implicates autophagy dysfunction at the core of this inflammatory condition, but the basis of this dysfunction is not fully understood. **Methods:** Using an *in vitro* model of lipid-laden macrophages, activity-based probes and high-throughput techniques, we studied the role of the cysteine proteases cathepsins in autophagy. **Results:** We showed that cathepsin activity is suppressed by oxidized lipids and that cathepsin has an indispensable role in the autophagy-lysosomal degradation pathway. Accordingly, loss of cathepsin function resulted in autophagy derangement. Shotgun proteomics confirmed autophagy dysfunction and unveiled a pivotal role of cathepsin L in a putative cathepsin degradation network. At the physiological level, cathepsin inhibition resulted in mitochondrial stress, which translated into impaired oxidative metabolism, excessive production of reactive oxygen species and activation of the cellular stress response, driven by ATF4-CHOP transcription factors. In addition, transcriptomic analysis of these cells uncovered some genetic similarities with the inflammatory macrophage phenotype (a.k.a M1

macrophages) and increased expression of inflammatory cytokines. **Conclusion:** Our data highlight the importance of cathepsins for mitochondrial quality control mechanisms and amelioration of vascular inflammation.

© 2019 The Author(s). Published by
Cell Physiol Biochem Press GmbH&Co. KG

Introduction

Cardiovascular diseases due to atherosclerosis are the primary cause of mortality in western countries [1]. A common cause of vascular injury is a perpetuated inflammatory response, mediated by the immune system towards modified lipoproteins under the vascular endothelium [2, 3]. Over time, persistent inflammatory activity can damage the structure of the blood vessel and can lead to the clinical manifestations of vascular complications such as heart attack and stroke [2].

Macrophages are key mediators of vascular inflammation and regulate arterial remodeling by secreting inflammatory cytokines and proteases such as cysteine cathepsins [4]. In particular, cathepsins B, L and S (hereafter referred to as cathepsins) are over-expressed in advanced arterial lesions and display abnormal activities compared to non-inflamed regions [5]. Likewise, animal models provide compelling evidence that cathepsins contribute to arterial plaque formation and underlie clinical events by extracellular matrix digestion, thereby rendering plaques prone to rupture [6].

Cathepsins are naturally expressed in the lysosomes of various cells and tissues, where the acidic environment provides the optimal conditions for their activity [7]. Lysosomes also mediate a variety of homeostatic processes such as nutrient breakdown and removal of damaged organelles, in a process uniformly termed as autophagy (macroautophagy) [8, 9]. During autophagy, cytoplasmic materials are carried and delivered by a double membrane vesicle (autophagosome) to the lysosomes, where a variety of hydrolases overtake cargo degradation [10]. Many cells exhibit basal autophagy activity under normal physiological conditions. However, in response to stress, autophagy is maximized to restore homeostasis and to curb the accumulation of potentially cytotoxic materials, thus enabling cell survival [8, 11]. Two distinct types of autophagy are recognized: “non-selective” and “selective” degradation. “Non-selective” or “bulk” degradation is frequently induced by nutrient depletion. “Selective” degradation involves sequestering of specific cellular targets under nutrient replete conditions [12, 13]. One of the best-characterized selective autophagy responses is mitophagy, which removes malfunctioning mitochondria [12]. The physical segregation of damaged mitochondria involves a coordinated remodeling process that generates small mitochondrial fragments. These are recognized by autophagy receptors such as p62 and shuttled to the lysosomes for degradation [14, 15]. This pathway of mitochondrial clearance is important in the context of cardiovascular diseases, since mitochondrial dysfunction is known to trigger vascular inflammation through various mechanisms [16, 17].

Whether cathepsins are dispensable to autophagy and mitochondrial quality control under conditions of metabolic stress is inconclusive. Yet, several reports suggest a possible link between cathepsin activity and proper mitochondrial function. For example, inhibition of cathepsins by a small molecule inhibitor increased reactive oxygen species (ROS) production in macrophages [18, 19]. Furthermore, in mouse embryonic fibroblasts, genetic ablation of cathepsin L was sufficient to induce mitochondrial superoxide production [20]. Nevertheless, a causative link between cathepsin inhibition and mitochondrial dysfunction has not been verified; and has not been explored in the context of hyperlipidemic stress. Here, we set out to study the role of cathepsins in autophagy using targeted chemical tools in conjunction with high throughput techniques such as proteomics and transcriptomics. We report that cathepsins temper macrophage inflammatory activity under hyperlipidemic stress by regulating lysosomal function and mitochondria quality control.

Materials and Methods

Animals

LDL receptor knockout mice (LDL^{-/-}) in the background of CL57BL/6 purchased from the Jackson Laboratory (Bar Harbor, ME USA) were housed in specific pathogen free conditions at the Hebrew University and were used with the approval of the animal ethics committee of the Hebrew University. Male mice, aged 6-12 weeks, were used for the experiments.

Isolation and preparation of human and mouse-derived macrophages

Human macrophages. Human macrophages were prepared from peripheral blood mononuclear cells (PBMCs) that were obtained from the blood of healthy donors by separation over Ficoll-Paque™ gradient (GE Healthcare, 17-1440-02). CD14 MicroBeads (Miltenyi Biotec, 130-050-201) were used for magnetic separation of monocytes. The cells were differentiated into macrophages over 7 days in RPMI media (Thermo Fisher Scientific, 21875034) containing 5% fetal bovine serum (Capricorn Scientific), 2mM L-glutamine (Thermo Fisher Scientific, 25030149), 1 mM non-essential amino acids (Thermo Fisher Scientific, 11140035), 1mM sodium pyruvate (Sigma-Aldrich, S8636), 1% penicillin/streptomycin (Thermo Fisher Scientific, 15140122) and 100 ng/ml recombinant human M-CSF (BioLegend, 574806). The cells were subsequently maintained in the same media with 10 ng/ml of M-CSF for the experiments.

Mouse bone marrow-derived macrophages. Bone marrow-derived macrophages (BMDM) were harvested according to Zhang *et al.* [21], with few modifications, and referred to as a “mixed population”. Briefly, bone-marrow cells were obtained from 5-7 mice (aged 8-10 weeks), mixed and allowed to differentiate into macrophages over 7 days in RPMI media (Gibco/Thermo Fisher Scientific, 21875) containing 10% fetal bovine serum (Biological industries, 04-127-1A), 2mM L-glutamine (Biological Industries, 03-022-1B), 1% penicillin/streptomycin (Biological Industries, 03-031-1B) and 50ng/mL M-CSF (Peprotech, 315-02). Afterwards, the media was changed and the cells were cultured for subsequent experiments using the same media formulation. For polarization experiments, the cells were treated with 20ng/mL LPS (Sigma-Aldrich, L4391) and 50ng/mL IFN- γ (Peprotech, 315-05) for 24 hours (h) for inflammatory M1 phenotype. For anti-inflammatory macrophages, M2, cells received 20ng/mL IL-4 (R&D Systems, 404-ML-010) for 24 h.

Cell culture and commercial reagents

Mouse macrophage cell line, Raw264.7 (American Type Culture Collection, TIB71TM), and NIH/3T3 embryonic fibroblasts (American Type Culture Collection, CRL-1658TM) were maintained in DMEM (Sigma-Aldrich, D5796), and supplemented as described for primary macrophages, but without M-CSF. All cell lines were negative for mycoplasma contamination (Biological Industries, 20-700-20). HBSS medium with calcium and magnesium is from (Gibco/Thermo Fisher Scientific, 14025092).

Lipid challenges

Cells were treated with 100 μ g/mL acetylated LDL (Biomedical Tech, BT-906) or 100 μ g/mL copper-oxidized LDL high TBAR (Biomedical Tech, BT-910X) for 24 h or 50 μ M 7-ketocholesterol (7-Keto), (Cayman Chemical, 16339), as indicated.

Autophagy, and the detection of organelles and ROS

Autophagy was determined using the autophagy detection kit (Abcam, ab139484) following the manufacturer's protocol. Chloroquine (CQ) 50 μ M (Sigma-Aldrich, C6628) was used to inhibit lysosomal activity for 2 h. Cells were stained using 50nM lysotracker green DND-26 (Fischer Scientific, L7526) or 100nM mitotracker green FM (Thermo Fisher Scientific, M7514) or 100nM mitotracker deep red FM (Cell Signaling Technologies, 8778). The trackers were active 30 min before analysis. For mitochondrial ROS (mtROS) detection, 1 μ M mitosox (Thermo Fisher Scientific, M36008) was used according to the manufacturer's protocol. N-acetyl-L-cysteine 10mM (Sigma-Aldrich, A7250) was used for ROS sequestering.

Mitochondrial metabolic analysis

Real time mitochondrial oxygen consumption was measured in Seahorse (Agilent) XF24 according to van den Bossche *et al.* [22], with few modifications. Briefly, 5x10⁴ cells were cultured in XF24-well plates in complete RPMI media, as described, and treated with GB11-NH₂ 10 μ M for 16 h or with DMSO as a control. Two

hours before the assay and mitochondrial respiration inhibitors (x10 stock solutions) were injected directly into RPMI media, 7-Keto (Cayman Chemical, 16339) 50 μ M was added, to obtain the final concentrations: 1.5 μ M oligomycin A (Sigma-Aldrich, 75351), 50 μ M carbonyl-cyanide 3-chlorophenylhydrazone, CCCP (Sigma-Aldrich, C2759), 1.25 μ M rotenone (Sigma-Aldrich, R8875) and 2.5 μ M antimycin A (Sigma-Aldrich, A8674). Data were normalized to the total protein content as determined by the BCA kit (Pierce™, 23225), and key metabolic features were calculated as described in van den Bossche *et al.* [22].

Cathepsin inhibition

The following inhibitors were used, 20 μ M cathepsin B inhibitor II (Calbiochem, 219385), 20 μ M cathepsin L inhibitor II (Calbiochem, 219426), indicated concentrations of cathepsin S inhibitor (Calbiochem, 219393) and 10 μ M of GB111-NH₂ [23]. Inhibitors were active 16 h prior to analysis.

Fluorescent gel scans and immunoblotting

Cathepsin activity was determined by fluorescent gel scans as described in [24], with several modifications. BMDM were cultured at a density of 1x10⁶ per well in 6-well plates one day before the experiments. Following 7-Keto treatments, BMDM were treated with GB123 [24] 1 μ M for 1 h followed by protein extraction in lysis buffer (25mM TRIS pH 7.4, 150mM NaCl, 1mM EDTA and 1% Triton-X100). Protein concentration was determined by the BCA kit from (Pierce™, 23225) and 25 μ g of total proteins were suspended in a Laemmli sample buffer and resolved on 12.5% SDS-PAGE. Gels were scanned by Typhoon FLA 9500 (GE Healthcare Life Science) and the Cy5 fluorescent signal intensity was quantified by ImageJ software (National Institute of Health). For western blots, protein extracts were prepared using lysis buffer as above and 50 μ g of total proteins were resolved on 12.5% SDS-PAGE. Proteins were then transferred onto a PVDF membrane (Bio-Rad) and incubated overnight at 4°C with primary antibodies diluted in TBSTx1 and 5% BSA fraction V (MP, 02160069). For immunoblots, the following antibodies were used: beta actin (Abcam, ab8227) 1:3000, SQSTM/p62 (Abcam, ab56416) 1:1000 and LC-3B (Abcam, ab51520) 1:1000. Membranes were then probed with secondary-HRP conjugated enzyme: goat anti-mouse (Bio-Rad, 170-6516) or goat anti-rabbit (Bio-Rad, 170-6515) at room temperature for another hour and a chemiluminescent signal was generated using the EZ-ECL kit (Biological Industries, 20-500-120). Blot images were taken by ChemiDoc XRS camera (Bio-Rad) and densitometric analyses were carried out using ImageJ software (National Institute of Health).

Immunofluorescence stains and microscopy analyses

Cells were seeded in 8-well cover slip chambers, μ -slides (iBidi, 80826) at a density of 2x10⁴ cells per well. For immunofluorescence stains, the following primary antibodies were used: LAMP-1 (Abcam, ab25245) 1:250, LC-3B (Abcam, ab51520) 1:200, SQSTM/p62 (Abcam, ab56416) 1:100 and TOMM20 (Abcam, ab56783) 1:250. All primary antibodies were diluted in Cas-Block™ (Thermo Fischer Scientific, 008120) and incubated overnight at 4°C after fixation and permeabilization in pre-chilled methanol for 10 min at -20°C. Cells were washed thrice with PBS x1 and then incubated with secondary fluorescent-conjugated antibodies: donkey anti-rat (Jackson, 712-165-153) 1:250, donkey anti-rabbit (Jackson, 711-165-152) 1:250 and donkey anti-mouse (Invitrogen, A21202) 1:250 in Cas-Block™ solution at room temperature for 1 h. Finally, unbound secondary antibody was removed by three successive washes with PBS x1 and the cells were mounted with DAPI-Fluoromount-G® (SouthernBiotech, 0100-20) before visualization by confocal microscopy FV3000 (Olympus), equipped with oil immersion objective lens x60 1.4NA. For experiments involving lipoproteins, macrophages were stimulated with 100 μ g/mL of acetylated LDL or oxidized LDL (oxLDL) for 24 h and then GB137 [24] 2 μ M was added for another 24 h. Cells were then prepared for confocal microscopy analysis as described. For experiments with 7-Keto, GB137 2 μ M was added for 8 h and the cells were processed for microscopy visualization. For mitochondrial stains, mitotracker deep red 100nM was added to the culture medium for 30 min at 37°C and the cells were then fixed in cold methanol and mounted with DAPI-Fluoromount-G® solution. Images were subsequently taken by inverted microscope IX83 (Olympus) equipped with oil immersion UPLSAPO x100 1.4NA objective lens. LC-3B and p62 were quantified by automatically counting on threshold images and dividing the total number of nuclei within each frame [25]. Colocalization analysis was done with CellProfiler [26] on threshold images. Mitochondrial morphology was determined according to [27, 28]. Image analyses and quantifications were done in ImageJ [29].

Real time quantitative PCR (qPCR)

RNA from mouse samples were prepared according to [30] using TRIzol™ reagent (Thermo Fischer Scientific, 15596026) according to the manufacturer's protocol. To improve RNA yields, NaCl was added to 2-propanol to a final concentration of 150mM during the RNA precipitation step. RNA (2µg) was then converted to cDNA using the high capacity cDNA reverse transcription kit (Thermo Fischer Scientific, 4368814). Samples (20ng per reaction) were analyzed using Syber green (Kapa Biosystems, KK4601) in iCycler-CFX real time PCR machine (Bio-Rad) and normalized to 36B4\RPLP0, a housekeeping gene. The qPCR primers available are listed in Supplementary Table 1 (for all supplementary material see www.cellphysiolbiochem.com). For primary human macrophages, total RNA was prepared using the miRNeasy Mini Kit (Qiagen, 217004) according to the manufacturer's instructions and 1µg of RNA was converted into cDNA using the Omniscript RT Kit (Qiagen, 205111). Marker expression was analyzed using the Luna Universal qPCR Master Mix (2X) (New England BioLabs, M3003) and the measurements were performed using the 7500 Real-Time PCR system (Applied Biosystems). Ribosomal protein *RPLP0* was used as a housekeeping gene for data normalization.

Flow cytometry analysis (FACS)

Organelle staining (e.g. mitotracker, mitosox and lysotracker) was carried out *in situ*, the media was removed followed by three successive washes with PBS x1. The cells were detached from the plates using a cell scraper and then re-suspended in cold PBS solution supplemented with 1% FBS. Mitotracker green FM (Thermo Fischer Scientific, M7514) and mitotracker deep red FM (Cell Signaling Technologies, 8778) were each applied at a 100nM final concentration for 30 min at 37°C. Lysotracker green DND-26 (Fischer Scientific, L7526) was applied at a 50nM final concentration for 30 min at 37°C. For mitochondrial superoxide production, mitosox 1µM in HBSS solution was applied to the cells for 15 min at 37°C according to the manufacturer's protocol. Extracellular marker stains were performed as described in [19] using the following dye-conjugated antibodies: CD206 (Biolegend, 141710) 1:500, F4/80 (eBioscience™, 17-4801-82) 1:500 and CD11b (eBioscience™, 17-0112-82) 1:500. After blocking non-specific targets, aliquots of 1x10⁶ cells in 0.5mL of cold FACS buffer (2mM EDTA and 1% FBS in PBS) were left for 30 min at room temperature and rotated with antibodies followed by three washing steps with PBS. Finally, cells were re-suspended in 1mL of cold FACS buffer and analyzed by flow cytometer. Data were attained using Cytotflex, flow cytometer (Beckman Coulter) and data were analyzed in CytoExpert 2 (Beckman Coulter).

Proteomics and data analysis

Preparation of samples for LC/MS/MS. Sample preparation and proteomic analysis were according to [31], with several modifications. Macrophages (5x10⁶ cells) were treated with GB111-NH₂ or DMSO for 16 h prior to the addition of 7-Keto. Proteins were extracted in 100µL of SDS lysis buffer (50mM TRIS pH 7.5, 2% SDS, 1mM EDTA and 150mM NaCl) and boiled at 95°C for 5 min. Buffer was exchanged to urea lysis buffer (50mM ammonium bicarbonate, 8M urea), by chloroform/methanol precipitation, and proteins (25µg) were reduced with 10mM dithiothreitol (Sigma-Aldrich, D9779) and alkylated with 20mM iodoacetamide (Sigma-Aldrich, I1149) for 1 h at room temperature. Unreacted iodoacetamide was quenched by the addition of 10mM dithiothreitol. Tryptic digestion was carried out with LysC (Wako Laboratory Chemicals, 125-05061) 1:50 overnight at 37°C, after which urea concentration was diluted 5 fold in 50mM ABC buffer to 0.8M, and trypsin, MS Grade (Thermo-Scientific, 90057) 1:25 was added for another 8 h. Digestion was stopped by adding 1% formic acid solution.

Desalting and preparation for LC/MS/MS. Tryptic digests were desalted on homemade C18 StageTips as described [32]. Peptides were passed over a 2-disc StageTip. After elution from the StageTips, samples were dried using a vacuum concentrator (Eppendorf) and the peptides were taken up in 0.1% formic acid solution (10 µL).

LC/MS/MS. Experiments were performed on an Orbitrap Elite instrument (Thermo, Michalski et al. 2012) that was coupled to an EASY-nLC 1000 liquid chromatography system (Thermo). The LC was operated in the one-column mode. The analytical column was a fused silica capillary (75 µm × 36 cm) with an integrated PicoFrit emitter (New Objective) packed in-house with Reprosil-Pur 120 C18-AQ 1.9 µm. The analytical column was encased by a column oven (Sonation) and attached to a nanospray flex ion source (Thermo). The column oven temperature was adjusted to 45°C during data acquisition. The LC was equipped with two mobile phases: solvent A (0.1% formic acid, FA, in water) and solvent B (0.1% FA in acetonitrile, ACN).

All solvents were of UHPLC (ultra-high-performance liquid chromatography) grade (Sigma). Peptides were directly loaded onto the analytical column with a maximum flow rate that would not exceed the set pressure limit of 980 bar (usually around 0.5 – 0.8 $\mu\text{L}/\text{min}$). Peptides were subsequently separated on the analytical column by running a 140 min gradient of solvent A and solvent B (starting with 7% B; gradient 7% to 35% B for 120 min; gradient 35% to 100% B for 10 min and 100% B for 10 min), at a flow rate of 300 nl/min . The mass spectrometer was operated using Xcalibur software (version 2.2 SP1.48). The mass spectrometer was set in the positive ion mode. Precursor ion scanning was performed in the Orbitrap analyzer (FTMS; Fourier Transform Mass Spectrometry) in the scan range of m/z 300-1800 and at a resolution of 60000, with the internal lock mass option turned on (lock mass was 445.120025 m/z , polysiloxane) [33]. Product ion spectra were recorded in a data dependent fashion in the ion trap (ITMS; Ion Trap Mass Spectrometry), in a variable scan range and at a rapid scan rate. The ionization potential (spray voltage) was set to 1.8 kV. Peptides were analyzed using a repeating cycle consisting of a full precursor ion scan (1.0×10^6 ions or 30 ms) followed by 15 product ion scans (1.0×10^4 ions or 50 ms), where peptides are isolated based on their intensity in the full survey scan (threshold of 500 counts) for tandem mass spectrum (MS2) generation that permits peptide sequencing and identification. CID (collision-induced dissociation) collision energy was set to 35% for the generation of MS2 spectra. During MS2 data acquisition, dynamic ion exclusion was set to 60 seconds, with the maximum list of excluded ions as 500 members and with a repeat count of one. Ion injection time prediction, preview mode for the FTMS, monoisotopic precursor selection and charge state screening were enabled. Only charge states higher than 1 were considered for fragmentation.

Peptide and protein identification using MaxQuant. RAW spectra were submitted to an Andromeda [34] search in MaxQuant (version 1.5.3.30) using the default settings [35]. Label-free quantification and match-between-runs were activated [36]. MS/MS spectra data were searched against the Uniprot Mus musculus reference database (UP000000589_10090.fasta, 50717 entries, downloaded 3/17/2016). Enzyme specificity was set to "Trypsin/P". The instrument type in Andromeda searches was set to Orbitrap and the precursor mass tolerance was set to ± 20 ppm (first search) and ± 4.5 ppm (main search). The MS/MS match tolerance was set to ± 0.5 Da. The peptide spectrum match false discovery rate (FDR) and the protein FDR were set to 0.01 (based on the target-decoy approach and the decoy mode "revert"). The minimum peptide length was 7 amino acids. Label-free protein quantification was switched on, and unique and razor peptides were considered for quantification, with a minimum ratio count of 2, as predetermined by MaxQuant. Retention times were recalibrated based on the built-in nonlinear time-rescaling algorithm. MS/MS identifications were transferred between LC-MS/MS runs with the "match between runs" option, in which the maximal match time window was set to 0.7 min and the alignment time window set to 20 min. The quantification is based on the "value at maximum" of the extracted ion current. Modified peptides were allowed for quantification. The minimum score for modified peptides was 40. The number of biological replicates analyzed by label free proteomics were as follows: $n=5$ for DMSO, $n=6$ for GB111-NH₂, $n=3$ for 7-Keto, $n=3$ for 7-Keto + GB111-NH₂.

Data availability. The mass spectrometry proteomics data have been deposited to the ProteomeXchange Consortium via the PRIDE [37] partner repository (<https://www.ebi.ac.uk/pride/archive/>) with the dataset identifier PXD010497. During the review process, the data can be accessed via a reviewer account (Username: reviewer92067@ebi.ac.uk; Password: Fz05Pe9r).

Data analysis. The list of identified proteins generated by MaxQuant was loaded into Perseus (version 1.5.2.6). Comparison of protein group quantities (relative quantification) between different MS runs is based solely on the LFQ's as calculated by MaxQuant (MaxLFQ algorithm). The list was filtered for proteins with at least three valid values in each group. Subsequently, missing values were imputed, with values representing a normal distribution around the detection range of the mass spectrometer. Accordingly, means and standard deviations of the measured intensities were determined and a new distribution with a downshift of 1.8 standard deviations and a width of 0.3 standard deviations was generated. Subsequent statistical analyses and graphs were carried out in R (version 3.4.0) and Rstudio (version 1.0.143). Principal component analysis (PCA) was computed using the standard R statistical environment. PCA and volcano plots were both created with ggplot2. Protein network analysis was curated using Genmania [38] and visualized by the Statnet package [39] in R and Rstudio. Differentially expressed proteins were determined with the Limma package [40, 41], by setting a threshold for Log₂ difference greater than 1 or smaller than -1 and a FDR < 0.1.

RNA sequencing (RNA-seq) library preparation and data analysis

RNA (25–50 ng) molecules from a mixed donor population were fragmented by adding 5 fragmentation buffer (200 mM Tris acetate, pH 8.2, 500 mM potassium acetate and 150 mM magnesium acetate) and heating at 94°C for 3 min in a thermocycler followed by ethanol precipitation with ammonium acetate and GlycoBlue (Life Technologies) as carrier. Fragmented RNA was further processed using the Ovation® mouse RNA-Seq Systems (Nugen) according to the instructions of the manufacturer. This library preparation includes reverse transcription using random priming, second strand synthesis, blunt end repair, adapter ligation with nucleotide analog-marked adaptors, strand selection and insert dependent adapter cleavage (inDA-C) to remove rRNA, globin, and other housekeeping transcripts. Target sequences for inDA-C were derived from human sequences. The barcoded libraries were purified and quantified using the Library Quantification Kit - Illumina/Universal (KAPA Biosystems). A pool of up to 10 libraries was used for cluster generation at a concentration of 10nM using an Illumina cBot. Sequencing of 2x100 bp was performed with an Illumina HiScanSQ sequencer at the sequencing core facility of the IZKF Leipzig (Faculty of Medicine, University Leipzig) using version 3 chemistry and flow-cell according to the instructions of the manufacturer. Deep sequencing data of total-RNA with 101-bp paired-end, was de-multiplexed and raw data of each sample were quality checked (FastQC, v.0.11.5). After low quality bases were trimmed off, adapter sequences were clipped (cutadapt, v.1.14) and filtered reads were further quality checked. Remaining reads were uniquely aligned against the mouse genome (UCSC mm10 assembly) performed by HISAT2 (v.2.1.0) [42] for total-RNA reads. Subsequently, mapped reads were sorted and indexed (samtools, v.1.5) [42]. Annotation (featureCounts, v.1.5.3) [43] of total-RNA reads was performed against exonic regions of the mouse genome annotation (Ensembl, genome-build GRCh38.79). Resulting count data were normalized by the weighted trimmed mean of M-values (TMM) method, scaling sizes for each library [44]. Normalized read counts were converted to normalized fragments per kilobase per million (FPKM) mapped reads for paired-end reads of total-RNA; and to counts per million (CPM) mapped reads for single-end small-RNA reads. Subsequently read count data were tested for differential gene expression (DE), determined by edgeR (v.3.12.1) [45] in given conditions. Statistically significant DE was determined by a p-value of 0.05 using the FDR to correct for multiple testing. A multidimensional scaling plot was generated using the Limma package [40] in R. Pathway enrichment was determined based on the Gene Set Enrichment Analysis (GSEA) module in Webgestalt [46], using KEGG as the reference database.

Enzyme linked immunosorbent assay (ELISA)

TNF- α and MCP-1 were quantified using commercial ELISA kits from R&D systems® MT00B and MJE00B, respectively, according to the manufacturer's protocol. Briefly, 5x10⁶ BMDM were cultured and covered with 6 mL of complete media. After overnight incubation with stimuli, the supernatant was collected and filtered through 0.22 μ m PVDF membrane (Millipore). The supernatant was collected and kept at -80°C until analysis.

Statistical analysis

Statistical analyses were performed in Graphpad Prism 7 (GraphPad Software, Inc) or R (version 3.4.4) and Rstudio (version 1.0.143). Statistical significance was determined by Student's *t* test or Wilcoxon rank sum test (for data that did not follow a normal distribution). For multiple samples, one-way ANOVA was performed with Tukey or Dunnett post hoc corrections, or Kruskal-Wallis for non-parametric tests. Normality tests were done using the Shapiro-Wilk and D'Agostino-Pearson tests. *P* values below 0.05 were considered statistically significant unless stated otherwise. Biological replicates indicate the number of independent biological samples that were analyzed independently. The results are summarized over the number of independent experiments.

Statement of Ethics

For experiments involving human samples, all participants signed an informed consent. All animal studies conformed to internationally accepted standards and were approved by the institutional ethical committee.

Results

Cathepsin activity is induced by cholesterol in macrophage foam cells, but is suppressed by oxidized lipid metabolites

To begin to explore the role of cathepsins in autophagy under hyperlipidemic conditions, we established an *in vitro* model of macrophage foam cells, a *bona-fide* feature of the nascent plaque that was previously shown to induce autophagy [47]. To this end, we loaded primary bone marrow derived macrophages (BMDM) with acetylated LDL cholesterol (acLDL) and confirmed the formation of foam cells by oil red O stains (Supplementary Fig. 1a). Next, we verified the induction of autophagy under similar conditions in primary BMDMs and in the macrophage like cell line Raw264.7 by staining for LC-3B (autophagosomes), (Supplementary Fig. 1b and Supplementary Fig. 2). Since autophagy culminates in the fusion of autophagosomes with lysosomes, we investigated the effect of hyperlipidemia on lysosomal cathepsin activity. Specifically, we sought to determine the effect of oxidized lipids such as oxLDL on cathepsin function, as oxLDL is believed to trigger vascular inflammation [48]. BMDMs were stimulated with oxLDL or acLDL as control, and cathepsin activity was measured by the quenched fluorescent activity-based probe GB137 [24]. We found that acLDL stimulated cathepsin activity at 4 fold compared to controls, while this effect was remarkably attenuated (to 2 fold) by oxLDL (Fig. 1a, b). Since 7-Keto is the most abundant lipid metabolite in the oxLDL particle [49], we hypothesized that it might be responsible for the reduction in cathepsin activity. Thus, we measured the impact of 7-Keto on cathepsin activity over time using a fluorescent gel assay with GB123 [23]. Similar to our observations with oxLDL particles, 7-Keto attenuated cathepsin activity, and cathepsins B and L displayed a steep decline, up to 50% after two hours (Fig. 1c, d). Cathepsin S, however, demonstrated a similar trend but only after 8 hours of 7-Keto stimulation (Fig. 1c, d). Next, we examined the effect of 7-Keto, and consequently reduced cathepsin activity on lysosomal function. We therefore stimulated BMDMs with 7-Keto and reduced the amount of serum in the culture media to induce lysosomal cargo delivery. Then the fluorescent signal produced by GB137 was captured by microscopy, thus confirming that 7-Keto attenuated cathepsin activity (Fig. 1e, f). In addition, we observed an overt structural change of the lysosomes to large spherical shapes; this suggests reduced lysosomal function (Fig. 1e). This attribute of lysosomal expansion was also positively correlated with a significant increase in the lysotracker signal as measured by flow cytometry analysis (Fig. 1g), and by microscopy studies when cathepsin activity was dampened by an inhibitor (Supplementary Fig. 3a, c). Overall, these data demonstrate a temporal relationship between autophagy induction and cathepsin activity in lipid-laden macrophages and suggest that cathepsin inhibition by oxidized lipids could impair lysosomal function.

Impaired cathepsin function attenuates autophagic degradation

Autophagy has become recognized as a preventive mechanism that reduces cellular damage and vascular inflammation [17]. Previous studies demonstrated that genetic ablation of cathepsin L impaired lysosomal cargo degradation [20]. Likewise, we set out to explore the impact of cathepsin inhibition on autophagy in response to hyperlipidemic conditions in primary BMDMs. We therefore blocked cathepsin activity by the cathepsin inhibitor GB111-NH₂ [23] and added 7-Keto at different time points. In the next step, we monitored the dynamics of the autophagy markers LC-3B and p62 over time. We observed higher levels of LC-3B and p62 in GB111-NH₂ treated-BMDMs, even before the addition of 7-Keto. This suggests that baseline autophagic degradation is suppressed due to cathepsin inhibition (Fig. 2a-e and Supplementary Fig. 4a, b). Similarly, autophagic degradation induced by 7-Keto was markedly suppressed in these cells, as evident by the accumulation of LC-3B and p62 after 7-Keto (Fig. 2a-e), and also by autophagy flux analyses (Supplementary Fig. 4c-e). Furthermore, LC-3B expression increased after 7-Keto stimulation, regardless of cathepsin inhibition. We therefore hypothesized that GB111-NH₂ does not affect the initiation of autophagy, but rather acts downstream within lysosomes to impair autophagosome

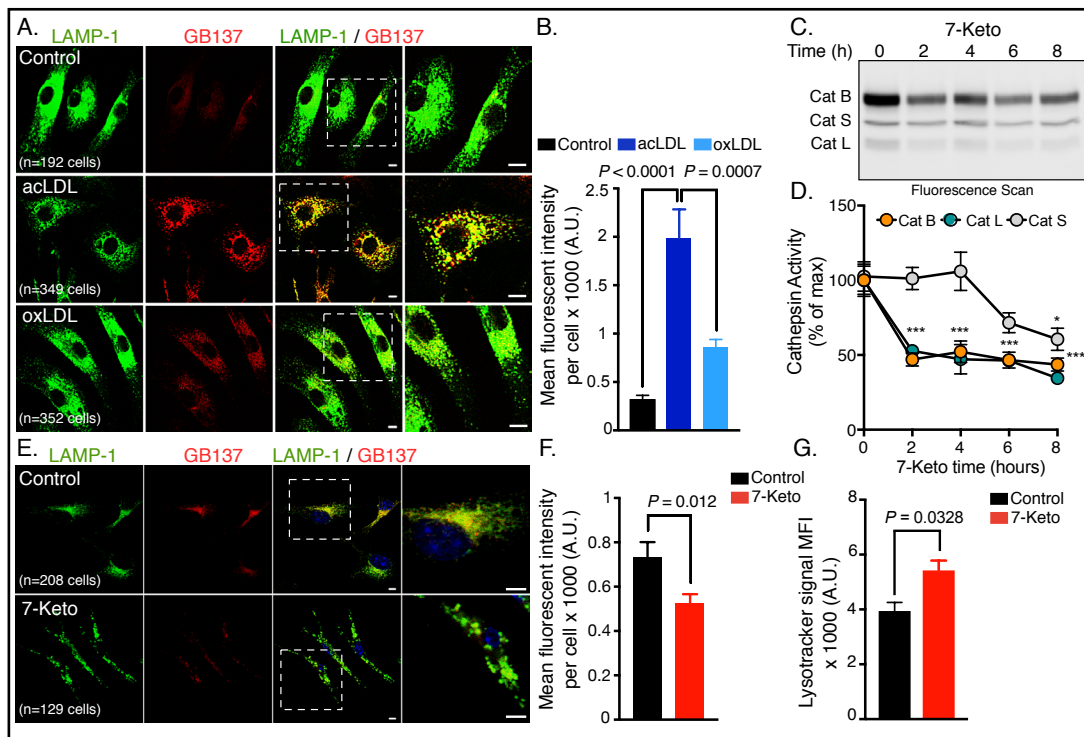


Fig. 1. Oxidized cholesterol attenuates cathepsin activity. Primary BMDMs were stimulated with modified cholesterol. (A) Confocal micrographs of BMDMs stimulated with cholesterol for 48 hours. LAMP-1 stains for lysosomes (green) and cathepsin activity (red), as indicated by GB137 fluorescent signal. (B) Quantification of the GB137 fluorescent signal from three independent experiments and subsequent one-way analysis of variance (ANOVA) with Tukey's corrections for multiple hypotheses performed to assess statistical difference. (C) Representative fluorescent gel scan (Ex/Em 532/580) and quantification (D) of BMDM cathepsin activity after 7-Keto stimulation at different time points. Data are expressed relative to unstimulated controls (time point 0) and one-way ANOVA with Tukey's post hoc analyses used to evaluate the statistical difference from three independent experiments. *, $P < 0.05$, ***, $P < 0.0001$. (E, F) Confocal images and quantification of lysosomal marker LAMP-1 (green) and cathepsin activity (red) in primary BMDMs with or without 8 hours of 7-Keto stimulation under low serum conditions (2% FBS). Cathepsin activity was monitored by the GB137 fluorescent signal and statistical differences were evaluated by two tailed Student's t-test from two independent experiments. (G) Flow cytometry analysis of lysotracker signal from three independent trials. Bar graphs present the mean \pm SEM. The scale bar is 5 μ m and 2.5 μ m for magnified images.

turnover (Fig. 2b). To examine this hypothesis, we measured the overlap between LC-3B and the lysosomal protein LAMP-1 at basal conditions and after 7-Keto stimulation. We found that cathepsin inhibition increased the overlap of LC-3B with the lysosomal marker LAMP-1 at baseline conditions and after four hours of 7-Keto treatment (Fig. 2f, g). This confirmed our hypothesis that cathepsins are instrumental to lysosomal turnover. Consistent with this hypothesis, NIH3T3 and cultured BMDMs both failed to degrade LC-3B and p62 under starvation conditions, which entail a potent autophagy stimuli, such as when cathepsins were blocked by GB111-NH₂ (Supplementary Fig. 4a, b). We therefore concluded that cathepsins are pivotal to the autophagy-lysosomal pathway by regulating lysosomal turnover.

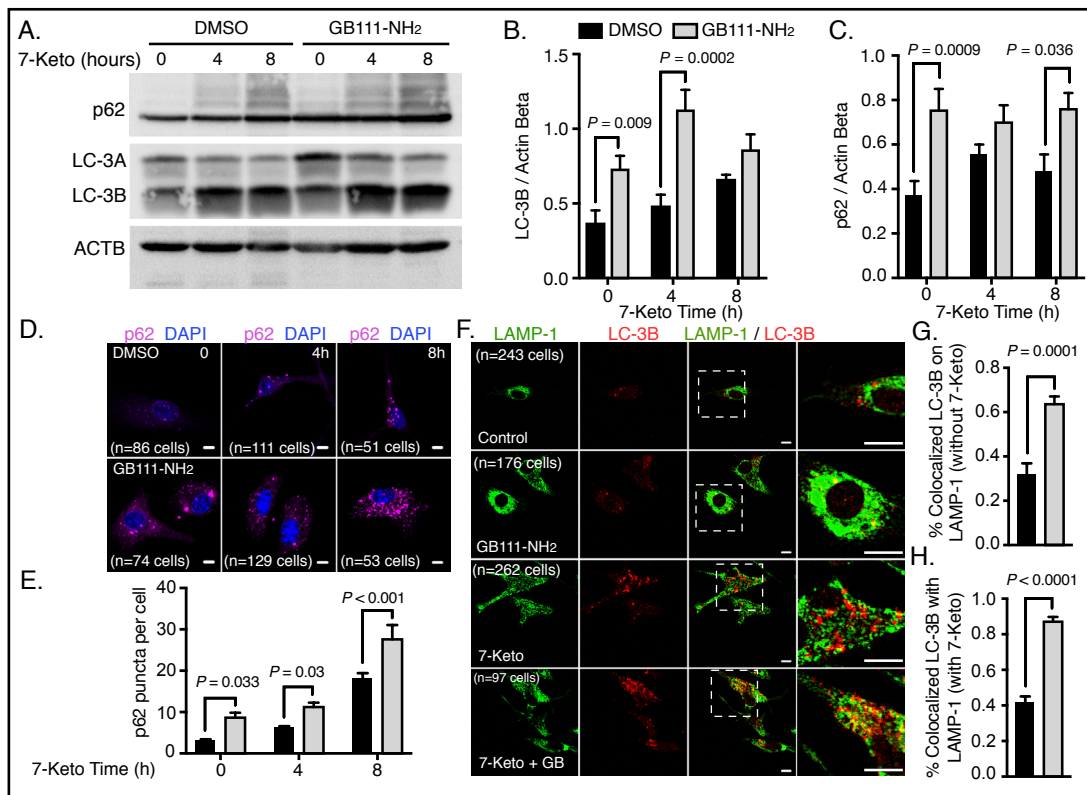


Fig. 2. GB111-NH₂ tampers with lysosomal activity and impairs autophagic degradation. (A) Primary BMDMs were treated with GB111-NH₂ or DMSO for 16 h followed by stimulation with 7-Keto for indicated times. Immunoblot of p62, LC3-A/B and beta actin from total cell lysate is presented. (B, C) Gel densitometry analyses of LC-3B and p62 normalized to beta actin from four independent trials. Two tailed Student's t-test was used to evaluate the statistical difference between GB111-NH₂ and DMSO for each time point, with the False Discovery Rate (FDR) post hoc correction for multiple comparisons. (D) Primary BMDMs were treated as described in panel A, fixed in cold methanol and stained with anti-p62 antibody (shown in purple) and DAPI (blue). (E) Quantification of microscopy data from two independent experiments. Statistical evaluation performed as described in panels B and C. (F) A representative confocal micrograph of immunofluorescence stains of LAMP-1 (green) and LC-3B (red) in BMDMs treated with GB111-NH₂ or DMSO, as described in (A) or after 4 h of 7-Keto treatment. (G, H) Data were quantified from three independent experiments presenting LC-3B colocalized with LAMP-1 without 7-Keto (G) or after 7-Keto stimulation (H). Bar graphs present the mean \pm SEM of DMSO (black bars) or GB111-NH₂ (gray bars) treated cells. Two tailed Student's t-test was used to determine statistical significance. The scale bar is 5 μ m and 2.5 μ m for magnified images.

Mass spectrometrical analysis reveals an important role for cathepsins in lysosomal function in BMDM cells

To extend our understanding on cathepsin function during autophagy, we implemented an unbiased shotgun proteomics approach as illustrated (Fig. 3a). This proteomic method led to the identification of 3255 proteins from the mouse proteome, in which we analyzed the impact of cathepsin inhibition on protein expression. Initially, we undertook an unsupervised learning approach, namely, PCA. This uncovered various expression patterns due to cathepsin inhibition (Fig. 3b). Targeted inspection of the autophagy markers, p62 (Sqstm1) and LC-3 (Map1LC3), confirmed that cathepsin inhibition attenuated autophagy turnover in this data set (Fig. 3d and Supplementary Table 2 and 3). Deeper examination of up-regulated proteins (e.g. up-regulated upon GB111-NH₂ treatment compared to DMSO) revealed 16 common proteins (displayed in a venn diagram) that were significantly changed regardless of 7-Keto stimulation (Fig. 3c). Since this protein set represents over 80% of

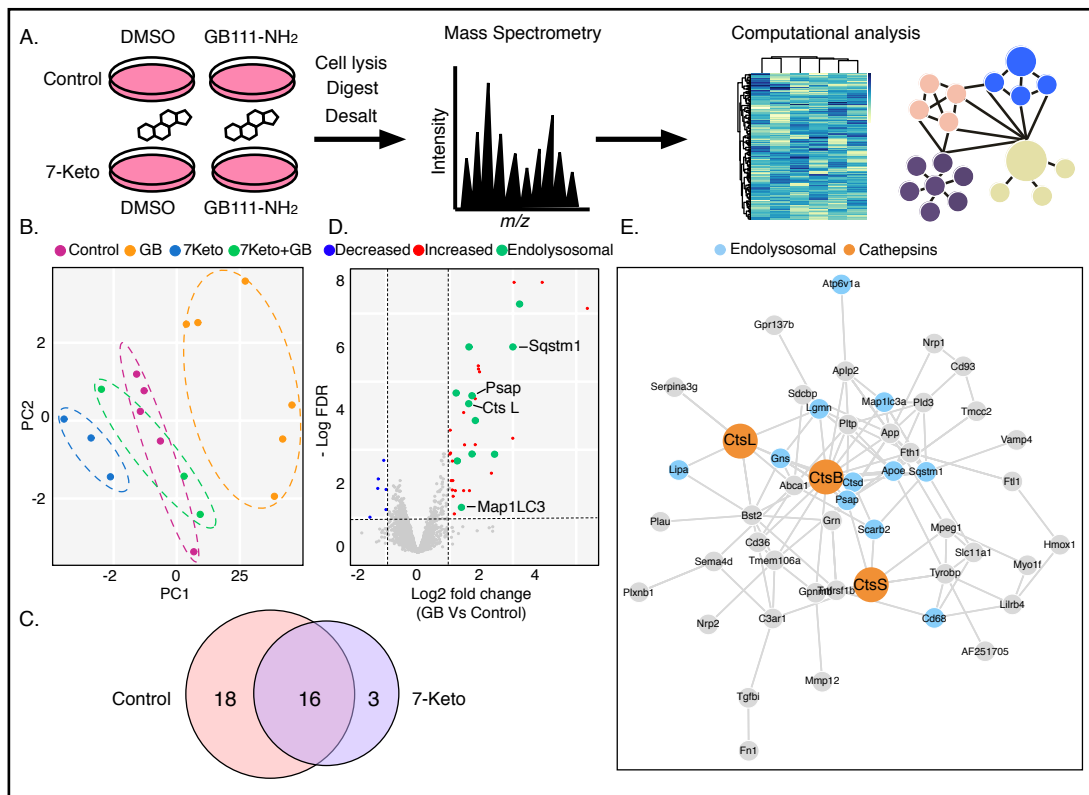


Fig. 3. Cathepsins are pivotal to lysosomal function. (A) Schematic description of experimental design. BMDMs were treated with GB111-NH₂ or DMSO vehicle for 16 h followed by 7-Keto or a vehicle for another 4 h. Cells were subsequently lysed and proteins were further prepared for mass spectrometry analyses. (B) Principal component analysis (PCA) of protein expression in BMDMs treated as described in panel A. Each point represents a biological replicate. (C) Venn diagram showing the overlap between up-regulated proteins (e.g. GB111-NH₂ vs. DMSO) in normal conditions or in response to 7-Keto. (D) Representative volcano plot showing differentially expressed proteins due to cathepsin inhibition by GB111-NH₂. Differentially expressed proteins (\log_2 fold change ± 1 and FDR < 0.1) represented by different colors (red, up-regulated, green, up-regulated endolysosomal, and blue, down-regulated protein expression). (E) Cathepsin-proteolytic network showing potential interactions and putative cathepsin targets.

the total differentially expressed proteins under 7-Keto-conditions (e.g. 19 proteins), we assumed that cathepsins regulate a similar set of biological processes. To further explore the biological processes that are regulated by cathepsins, we performed an enrichment analysis on a list of up-regulated proteins using the Kyoto Encyclopedia for Genes and Genomes (KEGG) pathways as a reference. We found enrichment for proteins constituting the lysosomal pathway, shown in green in the volcano plot (Fig. 3d, and Supplementary Tables 2 and 3). Finally, we were interested in exploring the relationship between cathepsins and the endolysosomal system, and in discovering potential novel protein targets. We therefore curated a theoretical cathepsin-proteolytic network based on existent data of physical interactions and colocalization (Fig. 3e). This network further confirmed that cathepsins play a key role in the endolysosomal system and suggested potential novel targets for cathepsins within this network (indicated in blue).

Next, we asked whether cathepsins are equally important in the lysosomal proteolytic network. We therefore simulated network-perturbation (*in silico*). This suggested that cathepsin L is a central modulator of this proteolytic network. To test this hypothesis, we evaluated the selectivity and potency of specific cathepsin inhibitors between the various cathepsins. Accordingly, BMDMs were treated with escalating doses of cathepsin inhibitors

and their remaining enzymatic activity was measured in tandem with the expression of LC-3B and p62. This assay revealed that the cathepsin L blockade was sufficient to cause lysosomal dysfunction, as evident by the dose-dependent relationships of cathepsin L inhibition with LC-3B and p62 protein levels (Supplementary Fig. 5a). Furthermore, we performed independent microscopy studies for p62 expression. These supported our observations, as cathepsin L blockade yielded p62 accumulation. This was exacerbated in the presence of 7-Keto (Supplementary Fig. 5b, c). Together, these data suggest that cathepsins are important to lysosomal function and support a key role for cathepsin L in this proteolytic system.

Mitochondria are targeted for lysosomal degradation by the autophagy machinery in response to 7-Keto

Our proteomic data demonstrated that the autophagy response induced by 7-Keto did not have a profound effect on the proteome level (data not shown). However, atherogenic lipids such as oxLDL and 7-Keto are known to inflict mitochondrial damage by elevating mitochondrial oxidative stress [16]. Consequently, damaged mitochondria are cleared by autophagy (mitophagy) to reduce cellular damage, and thus prevent inflammatory events and apoptosis [50]. Hence, we examined whether mitochondria are substrates for autophagic clearance under conditions of lipid overload. For this purpose, BMDMs were stimulated with 7-Keto and stained with LC-3B, p62 and the mitochondrial specific markers, Tomm20 and mitotracker deep red. We found that mitochondria were colocalized with LC-3B or the lysosomal marker LAMP-1 after 7-Keto stimulation (Supplementary Fig. 6a-c). Additionally, cathepsin inhibition augmented the association of mitochondrial markers with LC-3B and p62 (Fig. 4a-d). We also observed dense clusters of p62 on top of mitochondria, following GB111-NH₂ treatment. This implies slow protein turnover and possibly reduced mitochondrial clearance (Fig. 4b). These data suggest that the loss of cathepsin activity in the setting of hyperlipidemia forces macrophages to accumulate damaged mitochondria. Indeed, immunofluorescence and FACS analyses demonstrated that GB111-NH₂-treated BMDMs had increased mitochondrial content, as indicated by the fluorescent signals of the mitochondrial stains, Tomm20 and mitotracker green (Fig. 4e, f). Similarly, when we used CQ to block lysosomal activity, the mitotracker signal increased. In contrast, no change was observed when BMDMs were pre-treated with GB111-NH₂ (Fig. 4g). These findings suggest that cathepsins are essential to mitochondrial turnover by the lysosomes. We assumed that cathepsin inhibition would lead to the accumulation of mitochondrial damage under conditions of metabolic stress. We therefore assessed mitochondrial damage by FACS using double mitochondrial stains, mitotracker green (voltage independent) and mitotracker deep red (voltage dependent), as described previously [15, 51]. Consistent with our data, 7-Keto induced the appearance of damaged mitochondria (gated population), which was exacerbated by the presence of GB111-NH₂ or other lysosomal inhibitors such as cathepsin L inhibitor or CQ (Fig. 4h and Supplementary Fig. 6e). Overall, our data demonstrate that cathepsins are critical to mitochondrial clearance by autophagy in lipid-loaded macrophages.

Cathepsin inhibition alters mitochondrial dynamics and function

Mitochondrial dynamics has become recognized as a critical factor in the regulation of many aspects of mitochondrial health and function [52]. In various cell types, mitochondria are normally tubular, with interconnected branches that facilitate efficient metabolic function [52]. However, in response to mitochondrial damage, this versatile network rapidly changes and small-spherical fragments emerge, which are then cleared by the autophagy system [53]. The intimate link between mitochondrial dynamics, autophagy and the accumulation of damaged mitochondria resulting from cathepsin inhibition led us to investigate the impact of cathepsin inhibition on mitochondrial dynamics. To this end, BMDMs were stimulated by 7-Keto treatment at different time points and the resulting mitochondrial morphology was analyzed by fluorescence microscopy (Fig. 5a and Supplementary Fig. 7a). We observed that under normal culture conditions, BMDMs displayed dense clusters of tubular mitochondria (Fig. 5a and Supplementary Fig. 7a). However, with the addition of 7-Keto, a gradual

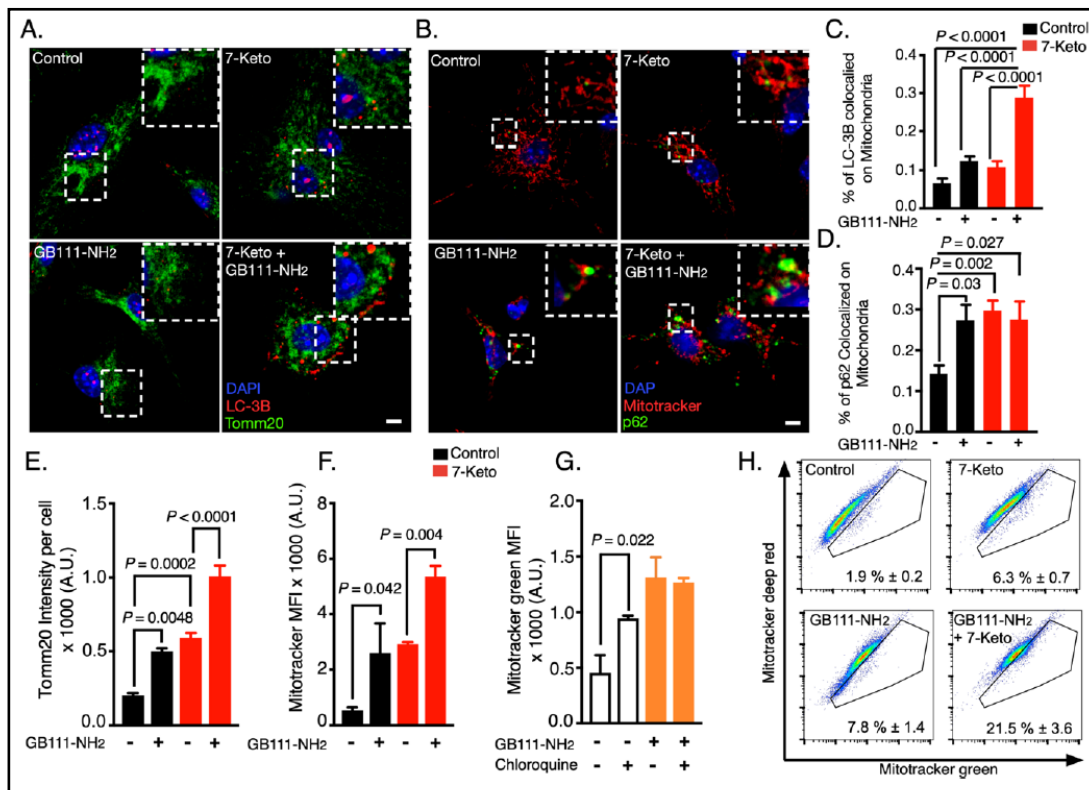


Fig. 4. Mitochondria are targeted for autophagic degradation by 7-Ketocholesterol (7-Keto). (A) Primary BMDMs were treated with GB111-NH₂ or DMSO for 16 h and then 7-Keto or vehicle were added for another 4 h. BMDMs were fixed and stained with LC-3B (red), Tomm20 (green) and DAPI for nuclei (blue). (B) BMDMs were treated as described in (A) and stained for p62 (green), mitotracker deep red (red) and DAPI (blue). (C, D) Colocalization analysis of LC-3B-Tomm20 and p62-mitotracker deep red, respectively. The data represent a summary of three independent experiments and one-way ANOVA with Tukey's correction for multiple hypotheses used to assess statistical difference. (E) Quantification of Tomm20 signal intensity from BMDMs treated with 7-Keto for 8 h after GB111-NH₂ pre-treatment, as described in panel A. One-way ANOVA with Tukey's correction for multiple hypotheses used to assess statistical significance. (F) Flow cytometry analysis of mitochondrial mass. BMDMs were treated with GB111-NH₂ or DMSO, as described in panel A and then stimulated with 7-Keto for another 4 h. During the last 30 min, mitotracker green was added and the cells were analyzed by flow cytometry. The data are summarized over three independent experiments and one-way ANOVA, with Sidak's correction for multiple hypotheses was used to assess statistical significance. (G) Flow cytometry analysis of mitochondrial mass, as described in panel F. BMDMs received chloroquine for 2 h prior to analysis. The data represent a summary of three biological replicates with one-way ANOVA, with Sidak's correction for paired comparisons. (H) Mitochondrial damage assessed by flow cytometry analyses. BMDMs were treated as described in (F) and stained with mitotracker green and mitotracker deep red prior to analysis. The gates represent cells with damaged mitochondria and the results are expressed as percentages of the total population. The data represent three independent experiments. Bar graphs present the mean \pm SEM.

increase in mitochondrial circularity was observed, which translated into the appearance of fragmented mitochondria (Fig. 5a-b and Supplementary Fig. 7a). Furthermore, we noted that cathepsin inhibition alone interfered with normal mitochondrial structure. This effect was intensified by the addition of 7-Keto, as evident by the frequency of small circular mitochondria (Fig. 5a-b). To further assess the contribution of cathepsins to mitochondrial morphology, we used JPM-OEt, an alternative pan cathepsin inhibitor and obtained similar results (Supplementary Fig. 6a-b). Hence, these data provide an intriguing link between cathepsins activity and mitochondrial quality control mechanisms.

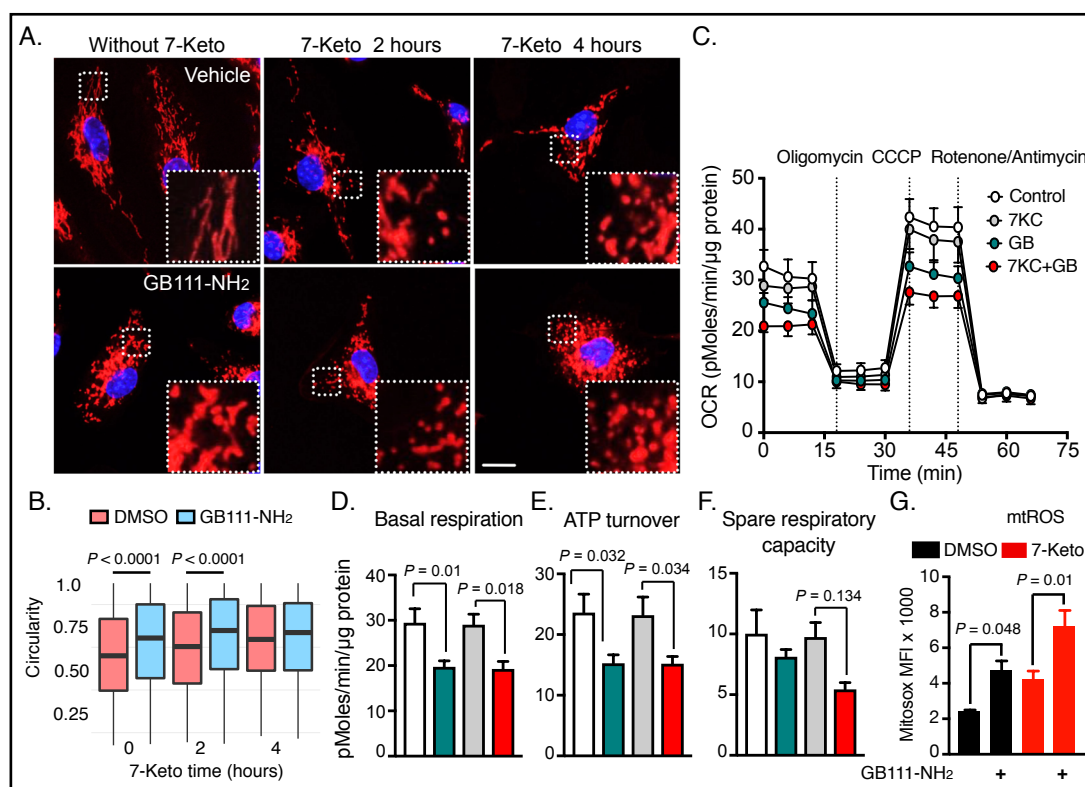


Fig. 5. Cathepsin inhibition causes mitochondrial dysfunction and alters its networked structure. Time resolved microscopy of mitochondrial structure in response to 7-Keto. (A) BMDMs were treated with GB111-NH₂ or DMSO for 16 h and then received 7-Keto or vehicle at the indicated time points. BMDMs were stained with mitotracker deep red for 30 min and fixed in cold methanol prior to microscopy examination (scale bar is 10 μm). (B) Mitochondrial circularity is presented in a box and whisker plot. One-way ANOVA with Tukey's post hoc test was used to compute statistical significance. The data represent a summary of three independent experiments. (C-F) Live cell mitochondrial-metabolic performance was measured using a Seahorse metabolic analyzer. BMDMs were cultured in assay plates and treated with GB111-NH₂ or DMSO as described in (A). 7-Keto was added two h before the metabolic assay. Real time oxygen consumption was measured by the Seahorse machine and respiratory performance was assessed as described in the Materials and Methods. Basal respiration, ATP turnover and spare respiratory capacity rates were inferred from the curve, normalized to total protein content and calculated as described in the Materials and Methods. Each assay contained 4-6 biological replicates, measured in three technical replicates. The data are summarized over 7 independent experiments. One-way ANOVA with Sidak's post hoc test was used to evaluate statistical significance. (G) Flow cytometry analysis of mitochondrial reactive oxygen species (mtROS) production. BMDMs were treated with GB111-NH₂ or DMSO as described in (A) and stimulated with 7-Keto for another 4 h. Mitoxox was used to evaluate mitochondrial ROS levels and measured by flow cytometry. One-way ANOVA and Tukey's post hoc test were used to compute statistical significance from three independent experiments. Bar graphs present the mean ± SEM.

Since mitochondrial networked-structure is considered advantageous to oxidative phosphorylation, we examined the effect of cathepsin inhibition on mitochondrial metabolic activity. Consistent with the changes in mitochondrial morphology, cathepsin inhibition reduced the mitochondria oxygen consumption rate and its coupling to ATP production before and after two hours of 7-Keto stimulation (Fig. 5c-e, Supplementary Fig. 7c). In addition, cathepsin inhibition reduced the mitochondrial spare respiratory capacity when loaded with 7-Keto (Fig. 5f). Since mitochondrial dysfunction is frequently associated with increased levels of mtROS, we measured mtROS production by flow cytometry. Lipid-loaded BMDMs generated significantly higher levels of mtROS when cathepsin activity was hindered

by small molecules (Fig. 5g and Supplementary Fig. 7d). Together, these data support the hypothesis that cathepsins are important for mitochondrial dynamics and for proper mitochondrial function.

Cathepsin inhibition promotes a pro-inflammatory phenotype and reduces anti-inflammatory markers in macrophages

Mitochondrial fragmentation has been demonstrated in astrocytes and in T cells following pro-inflammatory stimuli [53, 54]. Since mitochondrial fragmentation after GB111-NH₂ treatment was reminiscent of the phenotype observed in pro-inflammatory macrophages, and given that mitochondrial oxidative metabolism is a hallmark of anti-inflammatory macrophages [55], we considered whether GB111-NH₂ treatment could trigger a pro-inflammatory environment. First, we performed unbiased transcriptomic profiling in BMDM cells for different phenotypes, including M1 (inflammatory) and M2 (anti-inflammatory) polarization states. To this end, BMDMs were stimulated with LPS/IFN- γ for M1, IL-4 for M2, or with GB111-NH₂ or DMSO as a control. We then examined similarities and differences in the transcriptional profiles using a multi-dimensional scaling plot. As anticipated, M1 and M2 BMDMs were clearly distinguished from each other, while the DMSO and GB111-NH₂ treatments were closely related to M2 BMDMs (Fig. 6a). Interestingly, however, GB111-NH₂ treated BMDMs displayed some common transcriptomic features akin to M1 BMDMs, along the second dimension. This suggests that GB111-NH₂ induced transcriptional-reprogramming towards a pro-inflammatory state (Fig. 6a). Furthermore, analysis of differentially expressed genes between GB111-NH₂ and DMSO identified a transcriptional fingerprint of the integrated stress response spearheaded by ATF4 and CHOP, and their downstream targets (Fig. 6b). This transcriptional fingerprint is congruent with the mitochondrial dysfunction observed after GB111-NH₂ administration and concurs with observations by Quiros *et al.* [56]. The latter demonstrated induction of this stress-related pathway in response to mitochondrial damage. In addition, pathway enrichment using the KEGG database highlighted the induction of compensatory metabolic pathways, and also gene sets related to Parkinson and Huntington diseases, where lysosomal dysfunction is a key pathological feature (Fig. 6c).

Given the transcriptional programing described and the overt cell stress, we examined the expression of several inflammatory mediators by real time qPCR in BMDMs treated with GB111-NH₂. We found that IL-1 α , TNF- α and MCP-1 transcripts were significantly higher than DMSO controls. On the other hand, the expression of IL-6 remained unchanged (Fig. 6d). Most significantly, 7-Keto stimulated the secretion of MCP-1 and TNF- α , and GB111-NH₂ enhanced this effect (Fig. 6d, e). Altogether, these data suggest that cathepsin inhibition primes the inflammatory nature in BMDM.

To further evaluate the clinical effect of cathepsin inhibition, primary human macrophages derived from peripheral blood were treated with GB111-NH₂. Similarly, the inflammatory phenotype observed in mouse BMDMs was phenocopied, and demonstrated an increase in IL-1, IL-6, TNF and MCP-1, and also in iNOS and CCR7. This further substantiates the generality of these findings (Fig. 6e). In light of the contribution of cathepsin inhibition to mitochondrial dysfunction and the excess production of mtROS under hyperlipidemic conditions (Fig. 5g), we sought to determine whether mtROS could stimulate inflammatory cytokine expression in BMDMs. To this end, BMDMs were conditioned with GB111-NH₂ or DMSO, and treated with N-acetyl cysteine or vehicle to sequester ROS. Then, BMDMs were supplemented with 7-Keto and cytokine expression was measured by qPCR. In agreement with the inflammatory shift due to cathepsin inhibition, NAC effectively reduced the transcript levels of the aforementioned cytokines (Supplementary Fig. 8). This effect was mostly significant in the presence of 7-Keto and GB111-NH₂ (Supplementary Fig. 8). Taken together, these data suggest a cellular paradigm-shift towards a pro-inflammatory phenotype due to mitochondrial stress, driven by cathepsin inhibition.

We examined if GB111-NH₂ also intensifies inflammatory cytokine expression in response to the pro-inflammatory (M1) stimuli, INF- γ and LPS. Under these stimuli, the

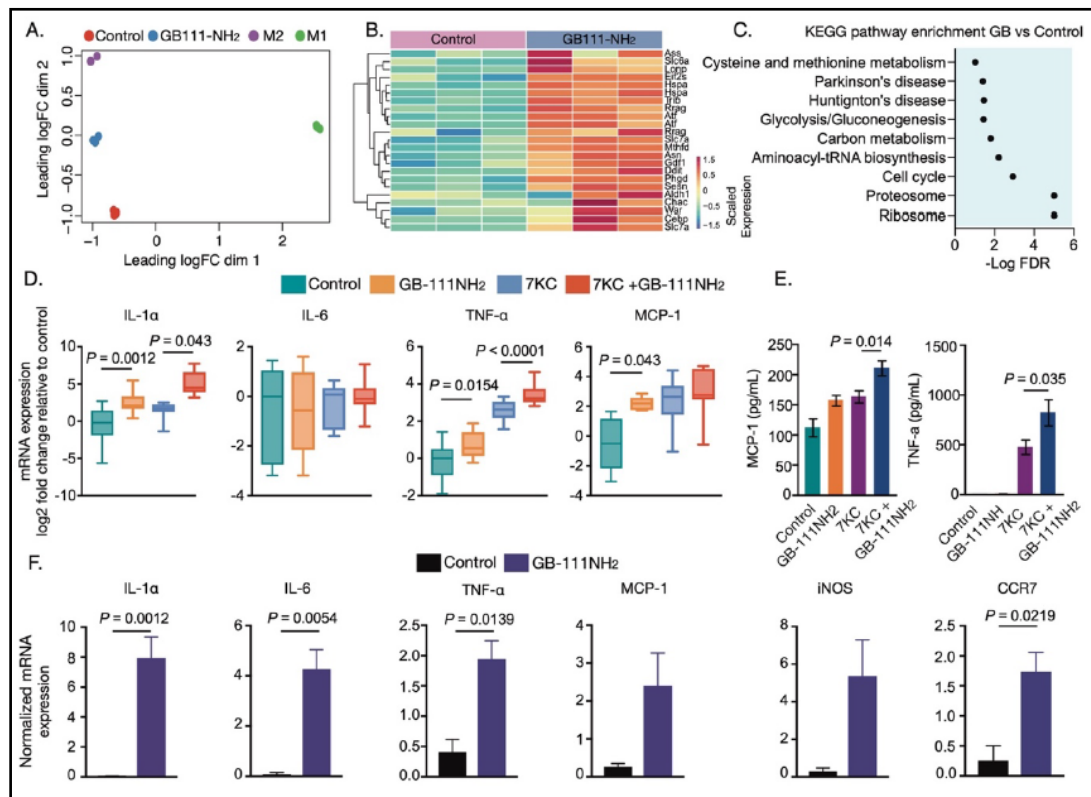


Fig. 6. Loss of cathepsin function promotes pro-inflammatory phenotype in macrophages. BMDMs were treated with GB111-NH₂ or DMSO for 16h or IL-4 for 24 h to induce the M2 phenotype, or LPS/IFN-γ for 24 h to generate the M1 phenotype. (A) Multi-Dimensional Scaling (MDS) plot from RNA-seq data showing distances between groups on a two-dimensional scale (n=3 biological replicates). (B) A heat-map presenting expression of stress related genes in GB111-NH₂ and DMSO vehicle treated BMDMs, as described in panel (A). (C) Gene Set Enrichment Analysis (GSEA) of KEGG pathways showing enriched gene sets in GB111-NH₂ treated BMDMs compared to DMSO controls. (D) BMDMs pre-treated with GB111-NH₂ or DMSO for 16 h were further stimulated with 7-Keto or vehicle for an additional 4 h (n=10-15 biological replicates from five independent experiments). The box and whisker plot presents log₂ fold changes compared to DMSO controls. The data are summarized over 15 biological samples per condition. The Kruskal-Wallis test was used to compute statistical significance. (E) Secretion of inflammatory cytokines is exacerbated by cathepsin inhibition upon stimulation with oxidized lipids. MCP-1 and TNF-α levels were determined by ELISA from the supernatant of BMDM cultured with different stimuli. The data were summarized from two independent experiments with 6 biological replicates. One-way ANOVA with Sidak's post hoc correction for multiple comparisons was used to evaluate the statistical difference between treatments. (F) Expression of inflammatory genes due to cathepsin inhibition in human primary macrophages (n=3 biological replicates). Macrophages were treated with GB111-NH₂ for 24h or with DMSO control. Normalized expressions of inflammatory genes are presented in bar graphs. Two-tailed Student's t-test was used to evaluate the statistical difference. Bar graphs present the mean ± SEM, and box and whiskers plot.

pattern of inflammatory gene expression (IL-6, TNFα, MCP-1 and iNOS) was comparable between GB111-NH₂ and controls, in both human and mouse primary macrophages (Fig 7a, b). However, in the mouse samples, we noted that GB111-NH₂ stimulated the expression of IL-1α, consistent with our observations in naïve BMDMs (Fig. 6d). In parallel, we examined the expression of anti-inflammatory markers in mouse M2 stimulated BMDMs, in the presence of IL-4, by qPCR and flow cytometry. Unlike with the M1 phenotype, here we observed a steep decline in Retnla and ARG-1 mRNA expression and surface expression of CD206 (Fig. 7c, d), and a moderated reduction in IL-10 and MRC-1 mRNA expression (Supplementary

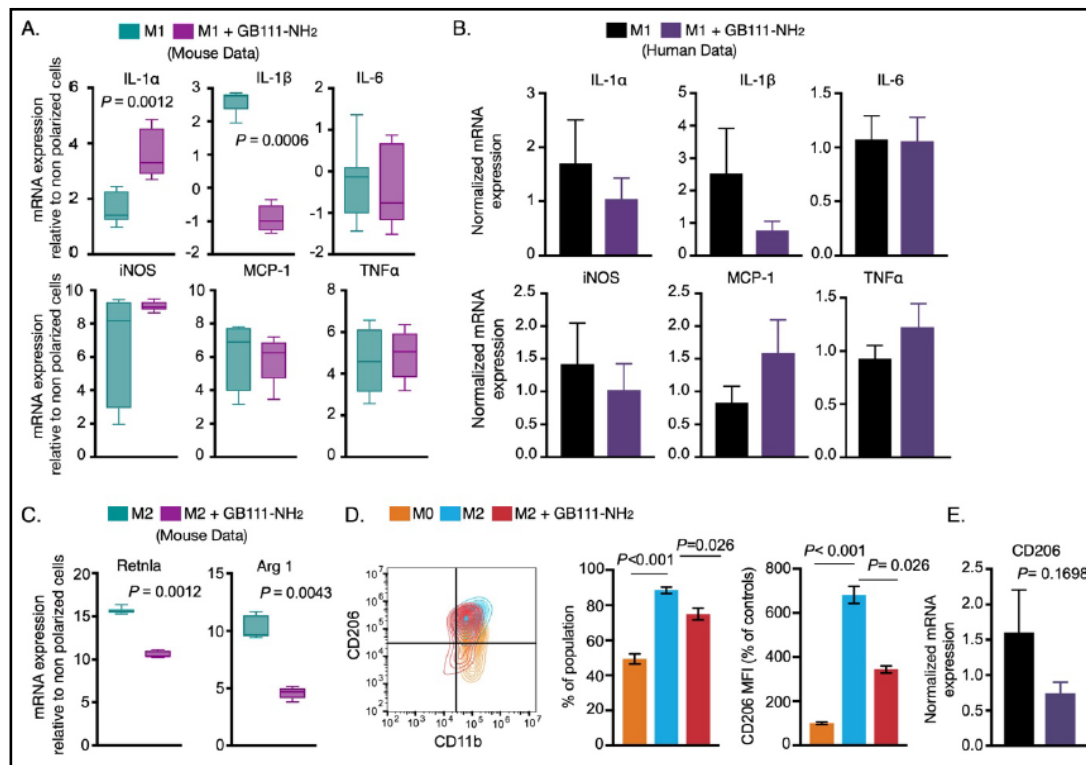


Fig. 7. Cathepsin dysfunction alters M2 phenotype. BMDMs were treated with GB111-NH₂ or DMSO vehicle for 16 h and then polarized with LPS/INF γ (M1) or with IL-4 for 24 h (M2, anti-inflammatory). (A) Normalized expression of inflammatory cytokines in M1 BMDMs are presented relative to non-polarized BMDMs (6 biological replicates from three independent experiments). The Wilcoxon rank sum test was used to evaluate statistical difference. (B) Human primary macrophages were pretreated with GB111-NH₂ or DMSO control for 24 h and polarized to generate M1 phenotype with LPS/INF γ . Normalized expressions of inflammatory genes are presented in the bar graph. The data are presented as mean \pm SEM (n=3 biological replicates). Student's t-test was used to evaluate statistical significance. (C) BMDMs were treated with GB111-NH₂ for 16 h, then polarized to yield M2 phenotype in the presence of IL-4 for another 24 h. Normalized expressions of classical M2 markers, Retnla and ARG-1 are expressed as fold changes relative to non-polarized samples (n=6 biological replicates from three independent experiments). The Wilcoxon rank sum test was used to evaluate statistical differences between samples. (D) Flow cytometry analysis of CD206 expression in M2 polarized BMDMs. Contour plot showing CD11b and CD206 expression in M2 polarized BMDMs or in untreated cells with M0 as controls. CD206 positive cells were quantified from CD11b positive cells and presented as percentages of the population. The intensity of CD206 was analyzed relative to untreated BMDMs (M0) and presented as the percentage of untreated cells. The data are summarized over three biological replicates from two independent experiments. One-way ANOVA with Sidak's post hoc correction for multiple comparisons was used to evaluate statistical differences between groups. (E) mRNA expression of CD206 in human primary macrophages is shown in the bar graph (n=3 biological replicates). Two-tailed Student's t-test was used to evaluate statistical difference. Bar graphs present the mean \pm SEM.

Fig. 9a). Consistent with these observations, we found a similar trend in CD206 mRNA expression in primary human macrophages (Fig. 7e). Collectively, these data suggest that cellular stress due to cathepsin inhibition, and possibly due to mitochondrial dysfunction, are key cellular events that suppress the anti-inflammatory phenotype in these cells. In support of this hypothesis, RNA-seq analysis of mice BMDMs uncovered a transcriptional fingerprint of the integrated stress response, which was independently validated by qPCR analyses (Supplementary Fig. 9b, c). In addition, pathway enrichment using the KEGG database suggested the potential integration of altered cell signaling events (mTOR signaling

pathway) and altered metabolic pathways (lipid biosynthesis) that could drive this cellular stress response (Supplementary Fig. 9d).

Discussion

The long-standing view of cathepsins as atherogenic factors is supported by a large body of work. Both murine models and human vascular tissues underscore the contribution of cathepsins to the long-term sequela of atherosclerosis, by regulating the extracellular constituents of the vascular lesion. The present study focused on the intracellular functions of cathepsins. The findings raise new insights on cathepsins as anti-inflammatory mediators and highlight their importance to autophagy during the early events of atherosclerotic lesion development. Most significantly, we discovered that blunted cathepsin activity in the setting of hyperlipidemia perturbs mitochondrial dynamics, increases mitochondrial damage and elicits an inflammatory response. We conclude from these data that dysfunctional cathepsin activity has a key role in nascent plaque development.

Using an *in vitro* model of BMDM foam cells, we were able to gain a deeper understanding of the role of cathepsins during the early events of vascular lesion development. A protective role for cathepsins was hypothesized based on previous studies that demonstrated that lysosomal activity is increased in BMDM foam cells and potentially protects them from apoptosis, by means of various mechanisms [47, 57]. Similarly, since cathepsins are lysosomal hydrolases, we suspected they may have a protective role under similar conditions. Comparable to Ouimet *et al.* [47], we observed a similar increase in autophagy in primary BMDMs and in a macrophage like cell line, Raw264.7 (Supplementary Fig. 1 and 2). This finding suggests a general response to cholesterol overload in macrophages. The simultaneous increase in cathepsin activity indicates that cathepsins are engaged in the autophagic response under hyperlipidemic conditions (Fig. 1 and Supplementary Fig. 3). While these observations were carried out using acLDL (native cholesterol), oxLDL is considered the main trigger of vascular inflammation [48]. In contrast to acLDL, oxLDL reduced cathepsin activity. In particular, we noted that 7-Keto, an abundant oxidized lipid, was sufficient to phenocopy this effect in a time dependent manner (Fig. 1).

While the basis for cathepsin inhibition by oxidized lipids requires further investigation, a possible mechanism could be a rise in lysosomal pH consequent to lipotoxicity. This is evident in other cell systems, such as pancreatic beta cells, hepatocytes and cardiomyocyte cells [58]. This surmise is consistent with the very rapid blunting of cathepsin B and L activity by 7-Keto, while its effect on cathepsin S was slower (Fig. 1).

Lysosomal degradation of autophagic cargo is the terminal step in autophagy. Lysosomal enzymes are commonly inhibited by alkalizing agents or broad cysteine/serine protease inhibitors in order to study the outcomes of lysosomal dysfunction in various models. Research from our laboratory and others [19, 20] suggests that cathepsin inhibition leads to autophagy dysfunction. However, this interpretation is not straightforward and could be context dependent. For example, a recent study by Qi *et al.* [59] demonstrated that genetic ablation or pharmacological inhibition of cathepsin B protects mice from *Francisella novicida* infection by enhancing its lysosomal degradation in a mechanism that involved the EB transcription factor. In the current work, we examined the effect of cathepsin inhibition on autophagy in a more rigorous manner. Using complementary approaches, we showed that cathepsin inhibition attenuates autophagic degradation by causing lysosomal dysfunction (Fig. 1 and 2 and Supplementary Fig. 4). Our observations that both LC-3B and p62 accumulate due to cathepsin inhibition with GB111-NH₂ and the attenuated flux in the presence of the general lysosomal inhibitor, CQ, confirms this paradigm (Fig. 2 and Supplementary Fig. 4) and concurs with other data sets [19, 20]. Further, unbiased mass-spectrometry analysis affirmed this hypothesis, and provides new insight into how cathepsins regulate lysosomal function under conditions of lipid-overload (Fig. 3).

Our data raise the intriguing possibility that cathepsins regulate lysosomal function through posttranslational modification of lysosomal hydrolases. This is because many of the differentially expressed proteins were annotated to the lysosomes. Our data indicate prosaposin as a putative cathepsin target (Fig. 3). Prosaposin is a lysosomal precursor for saposins A, B, C and D, which collectively facilitate the hydrolysis of glucoceramides. Mutations or deficiency in the saposin C gene are associated with abnormal accumulation of cytotoxic derivatives of ceramides and the lysosomal storage disease, Gauche. Previously reported data showed that excess dietary lipids altered lysosomal lipid composition and reduced its function [60, 61]. Hence, it is tempting to speculate that cathepsins regulate lysosomal activity by modulating its lipid composition. Another possibility is that impairment in the release of lysosomal calcium harms autophagosome-lysosome fusion, as suggested by Baixauli *et al.* [62].

Overall, our proteomic data demonstrate that a similar set of proteins is degraded by cathepsins under basal conditions and in response to stimulation with 7-Keto (Fig. 3). This is in line with the general model that under nutrient-replete conditions, autophagy mainly protects against organelle dysfunction [12]. As such, the mitochondria were attractive candidates, since previous studies showed that oxidized lipids, including oxLDL and 7-Keto, induced mtROS production [16]. Indeed, both autophagy markers, LC-3B and p62, were found in close proximity to mitochondria after 7-Keto stimulation. Notably, this stimulation was augmented in the presence of GB111-NH₂ (Fig. 4). Furthermore, the overall increase in mitochondrial mass and the accumulation of dysfunctional mitochondria is consistent with a uniform model in which cathepsin inactivation exacerbates mitochondrial dysfunction in the setting of hyperlipidemia.

How does cathepsin dysfunction contribute to elevated mitochondrial content? Intracellular mitochondrial content is dependent on the balance between mitochondrial biogenesis and mitochondrial clearance [63]. In the current study, the rapid increase in mitochondrial content (after 4 h of 7-Keto treatments) is less likely to be a consequence of increased mitochondrial biogenesis, even though we do not exclude this possibility [64]. Yet, a discriminative feature in the structural organization of the mitochondrial network was clearly visible between GB111-NH₂ and non-treated BMDMs (Fig. 5). Indeed, a significant increase in small-circular mitochondrial fragments was apparent in GB111-NH₂ treated cells. This indicates an increase in mitochondrial fragmentation and impaired mitochondrial turnover. The close relationship between mitochondrial structure and function recently elicited great interest in the context of immune function. The general framework is of an organized mitochondrial network that supports efficient oxidative metabolism. On the other hand, mitochondrial fragmentation that favors glycolytic metabolism was recently described in various immune cells including macrophages, astrocytes and T-cells [54, 65]. In consensus with this metabolic paradigm, we observed a decrease in oxidative metabolism due to cathepsin inhibition. This was exacerbated in the presence of 7-Keto (Fig. 5). Moreover, the parallel increase in the production of mtROS consolidates these observations and suggests that cathepsin inhibition reduces mitochondrial fitness and increases mitochondrial stress.

The molecular cues that drive mitochondrial fragmentation in the setting of cathepsin inhibition are currently unknown. However, an interesting possibility entails the involvement of the metabolic sensor AMP activated protein kinase (AMPK). AMPK is activated from a decrease in the energetic status of the cell, as can be induced by mitochondrial respiration inhibitors [53]. Under these circumstances, AMPK is engaged in a cell-signaling cascade that promotes mitochondrial fragmentation and facilitates its clearance via autophagy. Accordingly, AMPK acts as a feed-forward mechanism for mitochondrial fragmentation and dysfunction in the settings of cathepsin inhibition. However, future studies are needed to verify the likelihood of such mechanism.

Recently, comparable concentrations of GB111-NH₂ were found to attenuate glycolytic metabolism and to increase mtROS in LPS primed macrophages [18]. To circumvent the possibility that mtROS production in our study reflects changes in glycolytic metabolism rather than mitochondrial damage, we confirmed our findings that cathepsin inhibition

causes mitochondrial stress, also with other cathepsin inhibitors that are not known to affect glycolytic metabolism (Supplementary Fig. 7).

Oxidative stress ensuing from damaged mitochondria is a common driver of vascular inflammation. Our data show a consistent increase in the expression of IL-1 α , TNF α and MCP-1 due to cathepsin inhibition (Fig. 6). Recently, Childs *et al.* demonstrated a similar fingerprint of gene expression in senescent macrophage foam cells [66]. This is particularly interesting given the causative link between autophagy dysfunction and aging-related diseases. These could link between metabolic cathepsin dysfunction and premature aging. More importantly, Freigang *et al.* reported a critical role for IL-1 α in arterial plaque formation [67]. Our findings suggest a similar mechanism by which cathepsin dysfunction promotes vascular disorders by increasing IL-1 α in response to various stimuli, including classical inflammatory signals (Fig. 6). The mechanism by which cathepsin inhibition elicits IL-1 α expression is not addressed in the current study. However, both the work of Freigang *et al.* and our research suggest the involvement of mitochondrial dysfunction. In support of this mechanism, pre-treatment with the general ROS scavenger, N-acetyl cysteine could rescue this inflammatory phenotype in lipid-laden BMDMs.

It is well established that arterial plaques host a variety of leukocytes [3], including distinct types of macrophages, known as M1 and M2, with different inflammatory properties. While M2 induce anti-inflammatory activity, M1 promote inflammatory activity. A key difference between these two cell subtypes revolves around cellular metabolism. Whereas M1 display higher glycolytic activity, M2 rely heavily on oxidative metabolism. The overt perturbations to mitochondrial structure and the resultant decline in mitochondrial fitness prompted a closer look at the effect of cathepsin inhibition on BMDM polarization. Under inflammatory conditions, GB111-NH₂ did not show an additional effect on classical inflammatory markers, while it did increase IL-1 α expression (Fig. 7). Furthermore, we found that cathepsin inhibition had a profound impact on M2 polarization, as demonstrated by the reduction in classical M2 markers (Fig. 7) and as shown elsewhere [19].

Conclusion

In conclusion, this study demonstrated a key role for cathepsins in regulating vascular inflammation, and delineated intriguing crosstalk between cathepsin activity, autophagy, mitochondrial dysfunction and inflammation. Moreover, these data draw a clear line between the protective and side effects of cathepsin inhibition in the context of cardiovascular diseases. Nonetheless, this paper argues that intracellular cathepsin activity is mainly engaged in homeostatic processes such as mitochondrial quality control, and has a protective role. As others have shown, the extracellular activity of cathepsin appears to be the culprit of the devastating consequences of atherosclerosis complications.

Acknowledgements

The authors would like to acknowledge Dr. Knut Krohn from the University of Leipzig Core DNA Facility for preparing the RNA-seq libraries and handling the RNA-seq process.

Authors' contributions: T.W.S., I.G. and G.B. conceived the study. T.W.S., D.M., D.O., E.M. and A.A. performed the experiments. T.W.S., I.G., G.B., D.M., D.O., E.M., F.K. and A.A. analyzed the data. Y.B.N., D.T. and H.G. provided essential reagents for the study. F.K. performed proteomics experiments. D.M. analyzed RNA sequencing data. M.K., P.M., I.G. and G.B. oversaw the study. T.W.S., I.G., G.B., F.K., D.M., M.K., P.M., I.G. and G.B. wrote the manuscript.

The authors would like to thank the funding agencies, this work was supported by the United States–Israel Binational Science Foundation (2009010 and 2011480 to GB), the European Research Council Starting grant (337238 to GB) and the Deutsche Forschungsgemeinschaft (MI 710/8-1 to GB and PM).

Disclosure Statement

The authors have no conflicts of interest to declare.

References

- 1 Libby P, Bornfeldt KE, Tall AR: Atherosclerosis: Successes, Surprises, and Future Challenges. *Circ Res* 2016;118:531-534.
- 2 Back M, Weber C, Lutgens E: Regulation of atherosclerotic plaque inflammation. *J Intern Med* 2015;278:462-482.
- 3 Gotsman I, Sharpe AH, Lichtman AH: T-cell costimulation and coinhibition in atherosclerosis. *Circ Res* 2008;103:1220-1231.
- 4 Moore KJ, Tabas I: Macrophages in the pathogenesis of atherosclerosis. *Cell* 2011;145:341-355.
- 5 Abd-Elrahman I, Meir K, Kosuge H, Ben-Nun Y, Weiss Sadan T, Rubinstein C, Samet Y, McConnell MV, Blum G: Characterizing Cathepsin Activity and Macrophage Subtypes in Excised Human Carotid Plaques. *Stroke* 2016;47:1101-1108.
- 6 Kitamoto S, Sukhova GK, Sun J, Yang M, Libby P, Love V, Duramad P, Sun C, Zhang Y, Yang X, Peters C, Shi GP: Cathepsin L deficiency reduces diet-induced atherosclerosis in low-density lipoprotein receptor-knockout mice. *Circulation* 2007;115:2065-2075.
- 7 Stoka V, Turk B, Turk V: Lysosomal cysteine proteases: structural features and their role in apoptosis. *IUBMB Life* 2005;57:347-353.
- 8 Kroemer G, Marino G, Levine B: Autophagy and the integrated stress response. *Mol Cell* 2010;40:280-293.
- 9 Ohsumi Y: Molecular dissection of autophagy: two ubiquitin-like systems. *Nat Rev Mol Cell Biol* 2001;2:211-216.
- 10 Cuervo AM: Autophagy: in sickness and in health. *Trends Cell Biol* 2004;14:70-77.
- 11 Amaravadi R, Kimmelman AC, White E: Recent insights into the function of autophagy in cancer. *Genes Dev* 2016;30:1913-1930.
- 12 Evans TD, Sergin I, Zhang X, Razani B: Target acquired: Selective autophagy in cardiometabolic disease. *Sci Signal* 2017;10:pii:eaag2298.
- 13 Green DR, Levine B: To be or not to be? How selective autophagy and cell death govern cell fate. *Cell* 2014;157:65-75.
- 14 Shirihai OS, Song M, Dorn GW, 2nd: How mitochondrial dynamism orchestrates mitophagy. *Circ Res* 2015;116:1835-1849.
- 15 Zhong Z, Umemura A, Sanchez-Lopez E, Liang S, Shalpour S, Wong J, He F, Boassa D, Perkins G, Ali SR, McGeough MD, Ellisman MH, Seki E, Gustafsson AB, Hoffman HM, Diaz-Meco MT, Moscat J, Karin M: NF-kappaB Restricts Inflammasome Activation via Elimination of Damaged Mitochondria. *Cell* 2016;164:896-910.
- 16 Wang Y, Wang GZ, Rabinovitch PS, Tabas I: Macrophage mitochondrial oxidative stress promotes atherosclerosis and nuclear factor-kappaB-mediated inflammation in macrophages. *Circ Res* 2014;114:421-433.
- 17 Razani B, Feng C, Coleman T, Emanuel R, Wen H, Hwang S, Ting JP, Virgin HW, Kastan MB, Semenkovich CF: Autophagy links inflammasomes to atherosclerotic progression. *Cell Metab* 2012;15:534-544.
- 18 Sanman LE, Qian Y, Eisele NA, Ng TM, van der Linden WA, Monack DM, Weerapana E, Bogoy M: Disruption of glycolytic flux is a signal for inflammasome signaling and pyroptotic cell death. *Elife* 2016;5:e13663.
- 19 Salpeter SJ, Pozniak Y, Merquiol E, Ben-Nun Y, Geiger T, Blum G: A novel cysteine cathepsin inhibitor yields macrophage cell death and mammary tumor regression. *Oncogene* 2015;34:6066-6078.
- 20 Dennemarker J, Lohmuller T, Muller S, Aguilar SV, Tobin DJ, Peters C, Reinheckel T: Impaired turnover of autophagolysosomes in cathepsin L deficiency. *Biol Chem* 2010;391:913-922.
- 21 Zhang X, Goncalves R, Mosser DM: The isolation and characterization of murine macrophages. *Curr Protoc Immunol* 2008;Chapter 14:Unit 14.1.
- 22 Van den Bossche J, Baardman J, de Winther MP: Metabolic Characterization of Polarized M1 and M2 Bone Marrow-derived Macrophages Using Real-time Extracellular Flux Analysis. *J Vis Exp* 2015; DOI:10.3791/53424.

- 23 Blum G, Mullins SR, Keren K, Fonovic M, Jedeszko C, Rice MJ, Sloane BF, Bogyo M: Dynamic imaging of protease activity with fluorescently quenched activity-based probes. *Nat Chem Biol* 2005;1:203-209.
- 24 Blum G, von Degenfeld G, Merchant MJ, Blau HM, Bogyo M: Noninvasive optical imaging of cysteine protease activity using fluorescently quenched activity-based probes. *Nat Chem Biol* 2007;3:668-677.
- 25 Mizushima N, Yoshimori T, Levine B: Methods in mammalian autophagy research. *Cell* 2010;140:313-326.
- 26 Carpenter AE, Jones TR, Lamprecht MR, Clarke C, Kang IH, Friman O, Guertin DA, Chang JH, Lindquist RA, Moffat J, Golland P, Sabatini DM: CellProfiler: image analysis software for identifying and quantifying cell phenotypes. *Genome Biol* 2006;7:R100.
- 27 Marchi S, Bonora M, Patergnani S, Giorgi C, Pinton P: Methods to Assess Mitochondrial Morphology in Mammalian Cells Mounting Autophagic or Mitophagic Responses. *Methods Enzymol* 2017;588:171-186.
- 28 Ebrahimi-Fakhari D, Saffari A, Wahlster L, DiNardo A, Turner D, Lewis TL, Jr, Conrad C, Rothberg JM, Lipton JO, Kolker S, Hoffmann GF, Han MJ, Polleux F, Sahin M: Impaired Mitochondrial Dynamics And Mitophagy In Neuronal Models Of Tuberous Sclerosis Complex. *Cell Rep* 2016;17:2162.
- 29 Schindelin J, Arganda-Carreras I, Frise E, Kaynig V, Longair M, Pietzsch T, Preibisch S, Rueden C, Saalfeld S, Schmid B, Tinevez JY, White DJ, Hartenstein V, Eliceiri K, Tomancak P, Cardona A: Fiji: an open-source platform for biological-image analysis. *Nat Methods* 2012;9:676-682.
- 30 Gotsman I, Grabie N, Gupta R, Dacosta R, MacConmara M, Lederer J, Sukhova G, Witztum JL, Sharpe AH, Lichtman AH: Impaired regulatory T-cell response and enhanced atherosclerosis in the absence of inducible costimulatory molecule. *Circulation* 2006;114:2047-2055.
- 31 van den Boom J, Wolf M, Weimann L, Schulze N, Li F, Kaschani F, Riemer A, Zierhut C, Kaiser M, Iliakis G, Funabiki H, Meyer H: VCP/p97 Extracts Sterically Trapped Ku70/80 Rings from DNA in Double-Strand Break Repair. *Mol Cell* 2016;64:189-198.
- 32 Rappsilber J, Mann M, Ishihama Y: Protocol for micro-purification, enrichment, pre-fractionation and storage of peptides for proteomics using StageTips. *Nat Protoc* 2007;2:1896-1906.
- 33 Olsen JV, de Godoy LM, Li G, Macek B, Mortensen P, Pesch R, Makarov A, Lange O, Horning S, Mann M: Parts per million mass accuracy on an Orbitrap mass spectrometer via lock mass injection into a C-trap. *Mol Cell Proteomics* 2005;4:2010-2021.
- 34 Cox J, Neuhauser N, Michalski A, Scheltema RA, Olsen JV, Mann M: Andromeda: a peptide search engine integrated into the MaxQuant environment. *J Proteome Res* 2011;10:1794-1805.
- 35 Cox J, Mann M: MaxQuant enables high peptide identification rates, individualized p.p.b.-range mass accuracies and proteome-wide protein quantification. *Nat Biotechnol* 2008;26:1367-1372.
- 36 Cox J, Hein MY, Lubner CA, Paron I, Nagaraj N, Mann M: Accurate proteome-wide label-free quantification by delayed normalization and maximal peptide ratio extraction, termed MaxLFQ. *Mol Cell Proteomics* 2014;13:2513-2526.
- 37 Vizcaino JA, Csordas A, Del-Toro N, Dianas JA, Griss J, Lavidas I, Mayer G, Perez-Riverol Y, Reisinger F, Ternent T, Xu QW, Wang R, Hermjakob H: 2016 update of the PRIDE database and its related tools. *Nucleic Acids Res* 2016;44:11033.
- 38 Warde-Farley D, Donaldson SL, Comes O, Zuberi K, Badrawi R, Chao P, Franz M, Grouios C, Kazi F, Lopes CT, Maitland A, Mostafavi S, Montojo J, Shao Q, Wright G, Bader FD, Morris Q: The GeneMANIA prediction server: biological network integration for gene prioritization and predicting gene function. *Nucleic Acids Res* 2010;38:W214-20.
- 39 Handcock MS, Hunter DR, Butts CT, Goodreau SM, Morris M: statnet: Software Tools for the Representation, Visualization, Analysis and Simulation of Network Data. *J Stat Softw* 2008;24:1548-7660.
- 40 Ritchie ME, Phipson B, Wu D, Hu Y, Law CW, Shi W, Smyth GK: limma powers differential expression analyses for RNA-sequencing and microarray studies. *Nucleic Acids Res* 2015;43:e47.
- 41 Kammers K, Cole RN, Tiengwe C, Ruczinski I: Detecting Significant Changes in Protein Abundance. *EuPA Open Proteom* 2015;7:11-19.
- 42 Li H, Handsaker B, Wysoker A, Fennell T, Ruan J, Homer N, Marth G, Abecasis G, Durbin R, Genome Project Data Processing Subgroup: The Sequence Alignment/Map format and SAMtools. *Bioinformatics* 2009;25:2078-2079.
- 43 Liao Y, Smyth GK, Shi W: featureCounts: an efficient general purpose program for assigning sequence reads to genomic features. *Bioinformatics* 2014;30:923-930.
- 44 Robinson MD, Oshlack A: A scaling normalization method for differential expression analysis of RNA-seq data. *Genome Biol* 2010;11:R25.

- 45 Robinson MD, McCarthy DJ, Smyth GK: edgeR: a Bioconductor package for differential expression analysis of digital gene expression data. *Bioinformatics* 2010;26:139-140.
- 46 Wang J, Duncan D, Shi Z, Zhang B: WEB-based GENE SeT AnaLysis Toolkit (WebGestalt): update 2013. *Nucleic Acids Res* 2013;41:W77-83.
- 47 Ouimet M, Franklin V, Mak E, Liao X, Tabas I, Marcel YL: Autophagy regulates cholesterol efflux from macrophage foam cells via lysosomal acid lipase. *Cell Metab* 2011;13:655-667.
- 48 Sheedy FJ, Grebe A, Rayner KJ, Kalantari P, Ramkhalawon B, Carpenter SB, Becker CE, Ediriweera HN, Mullick AE, Golenbock DT, Stuart LM, Latz E, Fitzgerald KA, Moore KJ: CD36 coordinates NLRP3 inflammasome activation by facilitating intracellular nucleation of soluble ligands into particulate ligands in sterile inflammation. *Nat Immunol* 2013;14:812-820.
- 49 Jessup W, Kritharides L: Metabolism of oxidized LDL by macrophages. *Curr Opin Lipidol* 2000;11:473-481.
- 50 Galluzzi L, Kepp O, Kroemer G: Mitochondria: master regulators of danger signalling. *Nat Rev Mol Cell Biol* 2012;13:780-788.
- 51 Park SM, Ou J, Chamberlain L, Simone TM, Yang H, Virbasius CM, Ali AM, Zhu LJ, Mukherjee S, Raza A, Green MR: U2AF35(S34F) Promotes Transformation by Directing Aberrant ATG7 Pre-mRNA 3' End Formation. *Mol Cell* 2016;62:479-490.
- 52 Chan DC: Mitochondrial fusion and fission in mammals. *Annu Rev Cell Dev Biol* 2006;22:79-99.
- 53 Toyama EQ, Herzig S, Courchet J, Lewis TL, Jr., Loson OC, Hellberg K, Young NP, Chen H, Polleux F, Chan DC, Shaw RJ: Metabolism. AMP-activated protein kinase mediates mitochondrial fission in response to energy stress. *Science* 2016;351:275-281.
- 54 Motori E, Puyal J, Toni N, Ghanem A, Angeloni C, Malaguti M, Cantelli-Forti G, Berninger B, Conzelmann KK, Gotz M, Winklhofer KF, Hrelia S, Bergami M: Inflammation-induced alteration of astrocyte mitochondrial dynamics requires autophagy for mitochondrial network maintenance. *Cell Metab* 2013;18:844-859.
- 55 O'Neill LA: A Metabolic Roadblock in Inflammatory Macrophages. *Cell Rep* 2016;17:625-626.
- 56 Quiros PM, Prado MA, Zamboni N, D'Amico D, Williams RW, Finley D, Gygi SP, Auwerx J: Multi-omics analysis identifies ATF4 as a key regulator of the mitochondrial stress response in mammals. *J Cell Biol* 2017;216:2027-2045.
- 57 Liao X, Sluimer JC, Wang Y, Subramanian M, Brown K, Pattison JS, Robbins J, Martinez J, Tabas I: Macrophage autophagy plays a protective role in advanced atherosclerosis. *Cell Metab* 2012;15:545-553.
- 58 Trudeau KM, Colby AH, Zeng J, Las G, Feng JH, Grinstaff MW, Shirihai OS: Lysosome acidification by photoactivated nanoparticles restores autophagy under lipotoxicity. *J Cell Biol* 2016;214:25-34.
- 59 Qi X, Man SM, Malireddi RK, Karki R, Lupfer C, Gurung P, Neale G, Guy CS, Lamkanfi M, Kanneganti TD: Cathepsin B modulates lysosomal biogenesis and host defense against *Francisella novicida* infection. *J Exp Med* 2016;213:2081-2097.
- 60 Koga H, Kaushik S, Cuervo AM: Altered lipid content inhibits autophagic vesicular fusion. *FASEB J* 2010;24:3052-3065.
- 61 Rodriguez-Navarro JA, Kaushik S, Koga H, Dall'Armi C, Shui G, Wenk MR, Di Paolo G, Cuervo AM: Inhibitory effect of dietary lipids on chaperone-mediated autophagy. *Proc Natl Acad Sci U S A* 2012;109:E705-14.
- 62 Baixauli F, Acin-Perez R, Villarroya-Beltri C, Mazzeo C, Nunez-Andrade N, Gabande-Rodriguez E, Ledesma MD, Blazquez A, Martin MA, Falcon-Perez JM, Redondo JM, Enriquez JA, Mittelbrunn M: Mitochondrial Respiration Controls Lysosomal Function during Inflammatory T Cell Responses. *Cell Metab* 2015;22:485-498.
- 63 Dorn GW, 2nd, Vega RB, Kelly DP: Mitochondrial biogenesis and dynamics in the developing and diseased heart. *Genes Dev* 2015;29:1981-1991.
- 64 Gottlieb RA, Stotland A: MitoTimer: a novel protein for monitoring mitochondrial turnover in the heart. *J Mol Med (Berl)* 2015;93:271-278.
- 65 Buck MD, O'Sullivan D, Klein Geltink RI, Curtis JD, Chang CH, Sanin DE, Qu J, Kretz O, Braas D, van der Windt GJ, Chen Q, Huang SC, O'Neill CM, Edelson BT, Pearce EJ, Sesaki H, Huber TB, Rambold AA, Pearce EL: Mitochondrial Dynamics Controls T Cell Fate through Metabolic Programming. *Cell* 2016;166:63-76.
- 66 Childs BG, Baker DJ, Wijshake T, Conover CA, Campisi J, van Deursen JM: Senescent intimal foam cells are deleterious at all stages of atherosclerosis. *Science* 2016;354:472-477.
- 67 Freigang S, Ampenberger F, Weiss A, Kanneganti TD, Iwakura Y, Hersberger M, Kopf M: Fatty acid-induced mitochondrial uncoupling elicits inflammasome-independent IL-1 α and sterile vascular inflammation in atherosclerosis. *Nat Immunol* 2013;14:1045-1053.